UCSF
UC San Francisco Previously Published Works

Title

Computational pipeline provides mechanistic understanding of Omicron variant of concern neutralizing engineered ACE2 receptor traps.

Permalink

https://escholarship.org/uc/item/8nf664kq

Journal

Structure (London, England : 1993), 31(3)

ISSN

0969-2126

Authors

Remesh, Soumya G
Merz, Gregory E
Brilot, Axel F
et al.

Publication Date
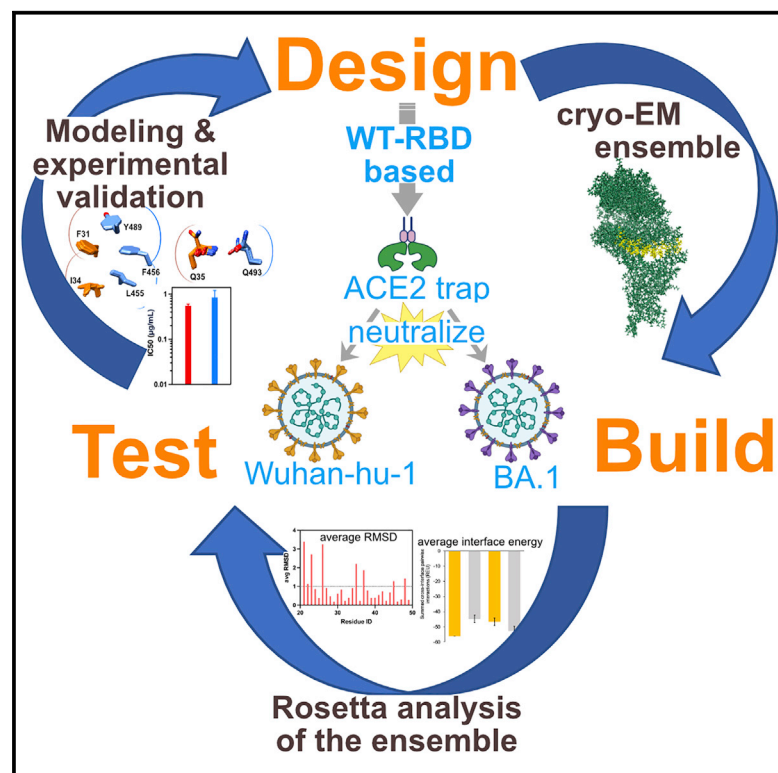
2023-03-01

DOI

10.1016/j.str.2023.01.009

Peer reviewed

Computational pipeline provides mechanistic understanding of Omicron variant of concern neutralizing engineered ACE2 receptor traps

Graphical abstract

Authors

Soumya G. Remesh, Gregory E. Merz, Axel F. Brilot, ..., Anum Glasgow, Kevin K. Leung, James A. Wells, Kliment A. Verba

Correspondence

ag4522@cumc.columbia.edu (A.G.),
kevin.leung@ucsf.edu (K.K.L.),
jim.wells@ucsf.edu (J.A.W.),
kliment.verba@ucsf.edu (K.A.V.)

In brief

With the emergence of new SARS-CoV-2 variants, there is a need for pan-variant Spike binders to inhibit viral entry. Using a novel pipeline combining cryo-EM and Rosetta, Remesh et al. characterize the mechanism of high-affinity interactions of designed ACE2 mimetic binders and show that they neutralize the Omicron variant.

Highlights

- Cryo-EM structure-based multi-model workflow with Rosetta interface energy metric

- Statistically averaged ACE2 receptor traps/WT-Spike interface side-chain positions

- Omicron-VOC neutralization by ACE2 receptor traps engineered against WT-Spike-RBD

CellPress

Article

Computational pipeline provides mechanistic understanding of Omicron variant of concern neutralizing engineered ACE2 receptor traps

Soumya G. Remesh,[1,2] Gregory E. Merz,[2] Axel F. Brilot,[2] Un Seng Chio,[2] Alexandrea N. Rizo,[2] Thomas H. Pospiech, Jr.,[2] Irene Lui,[1] Mathew T. Laurie,[3] Jeff Glasgow,[1] Chau Q. Le,[1] Yun Zhang,[1] Devan Diwanji,[2] Evelyn Hernandez,[2] Jocelyne Lopez,[2] Hevatib Mehmood,[2] Komal Ishwar Pawar,[2] Sergei Pourmal,[2] Amber M. Smith,[2] Fengbo Zhou,[2] QCRG Structural Biology Consortium, Joseph DeRisi,[3,4] Tanja Kortemme,[2,4,5,6,7] Oren S. Rosenberg,[2,4,10] Anum Glasgow,[8,*] Kevin K. Leung,[1,*] James A. Wells,[1,4,9,*] and Kliment A. Verba[2,5,9,11,*]

[1]Department of Pharmaceutical Chemistry, University of California, San Francisco, San Francisco, CA 94158, USA
[2]QBI Coronavirus Research Group Structural Biology Consortium, University of California, San Francisco, San Francisco, CA 94158, USA
[3]Department of Biochemistry and Biophysics, University of California, San Francisco, San Francisco, CA 94158, USA
[4]Chan Zuckerberg Biohub, San Francisco, CA 94158, USA
[5]QBI, University of California, San Francisco, San Francisco, CA 94158, USA
[6]Department of Bioengineering and Therapeutic Sciences, University of California, San Francisco, San Francisco, CA 94158, USA
[7]The University of California, Berkeley–University of California, San Francisco Graduate Program in Bioengineering, University of California, San Francisco, San Francisco, CA 94158, USA
[8]Department of Biochemistry and Molecular Biophysics, Columbia University, New York, NY 10032, USA
[9]Department of Cellular and Molecular Pharmacology, University of California San Francisco, San Francisco, CA 94158, USA
[10]Department of Medicine, University of California, San Francisco, San Francisco, CA 94143, USA
[11]Lead contact
*Correspondence: ag4522@cumc.columbia.edu (A.G.), kevin.leung@ucsf.edu (K.K.L.), jim.wells@ucsf.edu (J.A.W.), kliment.verba@ucsf.edu (K.A.V.)
https://doi.org/10.1016/j.str.2023.01.009

SUMMARY

The SARS-CoV-2 Omicron variant, with 15 mutations in Spike receptor-binding domain (Spike-RBD), renders virtually all clinical monoclonal antibodies against WT SARS-CoV-2 ineffective. We recently engineered the SARS-CoV-2 host entry receptor, ACE2, to tightly bind WT-RBD and prevent viral entry into host cells ("receptor traps"). Here we determine cryo-EM structures of our receptor traps in complex with stabilized Spike ectodomain. We develop a multi-model pipeline combining Rosetta protein modeling software and cryo-EM to allow interface energy calculations even at limited resolution and identify interface side chains that allow for high-affinity interactions between our ACE2 receptor traps and Spike-RBD. Our structural analysis provides a mechanistic rationale for the high-affinity (0.53–4.2 nM) binding of our ACE2 receptor traps to Omicron-RBD confirmed with biolayer interferometry measurements. Finally, we show that ACE2 receptor traps potently neutralize Omicron and Delta pseudotyped viruses, providing alternative therapeutic routes to combat this evolving virus.

INTRODUCTION

The rapidly evolving SARS-CoV-2 virus has accumulated several mutations throughout the pandemic. The Omicron variant, BA.1 (previously B.1.1.529), was first reported in November 2021 in South Africa to have 37 mutations in its Spike glycoprotein and was quickly designated as a variant of concern (VOC) by the World Health Organization.[1,2] The Omicron variant has now evolved to have several sub-variant members (BA.1, BA.1.1, BA.2, BA.3, BA.4, and BA.5) that have mutations in the receptor-binding domain (RBD) and N-terminal domain (NTD). The Omicron-Spike (S) glycoprotein of the variant BA.1 harbors 15 mutations in the RBD and 11 mutations in the NTD, respectively, leading to lower plasma neutralization in patients previously infected with

other SARS-CoV-2 variants or in fully vaccinated individuals.[3–10] Due to the antigenic shift in the Omicron variant, currently only two out of eight clinical monoclonal antibody treatments, S309 (sotrovimab parent) and the COV2-2196/COV2-2130 cocktail (cilgavimab/tixagevimab parents), retain appreciable neutralizing capacity albeit reduced by 2- to 3- and 12- to 200-fold, respectively, compared with neutralization of Wuhan-hu-1 strain.[3–8] An earlier VOC, the Delta variant, B.1.617.2, also acquired 10 mutations in the S glycoprotein, outcompeted other circulating virus isolates, and enhanced transmission and pathogenicity while diminishing antibody-based neutralization activity.[11,12] Interestingly, both the Delta- and Omicron-RBD continue to bind the SARS-CoV-2 entry receptor, human angiotensin-converting enzyme 2 (ACE2), with almost 2-fold higher affinity than the wild-type (WT)-RBD.[3,4]

Previously, we developed engineered ACE2 "receptor traps" as viable candidates for SARS-CoV-2 virus neutralization.[13] The receptor traps were computationally designed and further affinity-optimized by yeast display. The optimized ACE2 extracellular domains were fused to a human immunoglobulin (Ig)G1 Fc domain to afford additional binding avidity and neonatal Fc receptor (FcRN) binding for long circulating half-life. One advantage of using an ACE2 receptor trap as a therapeutic to treat SARS-CoV-2 infections is that resistance evolved to ACE2 traps would also likely render the virus unable to infect host cells via the ACE2 entry receptors. Thus, ACE2 traps could provide alternative therapeutic strategies for the rapidly evolving SARS-CoV-2 virus.

Our computationally designed (CVD293) and affinity matured (CVD313) ACE2 Fc-fusions have ~20- to 25-fold improved virus neutralization ability against WT-SARS-CoV-2 pseudotyped lentivirus (Wuhan-hu-1 strain) compared with the WT-ACE2 Fc-fusion.[13] However, the structures of neither CVD293 nor CVD313 bound to WT S protein have been captured, leaving it an open question as to why the affinity matured ACE2 receptor traps bind WT S protein tighter. Here, we shortened the length of the linker between the ACE2 extracellular domain (residues 18–740) of CVD313 and the Fc domain to 13 amino acids to generate the construct CVD432 and reverted the H345L mutation in CVD313 to WT residue, histidine. CVD432 also has the ACE2 native secretion signal that improved its mammalian expression profile (total yield post purification of CVD432 is ~2.5 times more than CVD313). We determined the cryoelectron microscopy (cryo-EM) structures of the stabilized ectodomain of S protein (residues 1–1,208, RRAR to GSAS mutation at residues 682–685 and KV to PP mutations at residues 986–987) with either CVD293 or CVD432, which revealed molecular details of the interactions between the ACE2 receptor traps and S protein. Building on previous approaches to provide ensemble models from cryo-EM maps,[14] we developed a multi-model workflow to improve our confidence in the molecular interactions and the interaction energies of the ACE2/RBD. This analysis allowed us to detect subtle interface differences between the two receptor traps that were critical for the improved ACE2/RBD interface. Furthermore, we used the cryo-EM structures together with Rosetta interface energy calculations to model the interactions between our ACE2 receptor traps and Spike-RBD of Omicron-VOC of SARS-CoV-2, rapidly identifying the direct contact residues and predicting an even tighter interaction than to the Wuhan-hu-1 S protein. We validated these structural modeling results by performing biolayer interferometry measurements. Finally, we showed that our ACE2 receptor traps potently neutralize Delta- and Omicron-SARS-CoV-2 pseudotyped viruses and thus can serve as alternate therapeutic candidates against SARS-CoV-2 infections.

RESULTS

Cryo-EM reconstructions of S protein trimer in complex with engineered ACE2 receptor traps

To understand the molecular details of the interactions between the S protein and the engineered ACE2 receptor traps CVD293 and CVD432, we determined the cryo-EM structures of these complexes (Figure 1). We confirmed that both CVD293 and CVD432 potently neutralize WT-SARS-CoV-2 (Wuhan-hu-1 B.1 strain with D614G mutation only) pseudotyped virus (Figure S1D

and Table S4). As noted previously for the S protein/WT-ACE2 complex,[15,16] we observed conformational heterogeneity for the complexes between S protein and the engineered ACE2 receptor traps, with the number of RBDs in the "up" or "down" conformation per S protein varying in the ACE2-bound state. The complex between S protein and CVD293 showed a 1-RBD-up S protein with full ACE2 occupancy (~20%), an appreciable percentage of 1-RBD-up S protein with partial ACE2 occupancy (~54%), a 2-RBD-up state with 1-ACE2 occupancy (~15%), and a 1-RBD-up state with no ACE2 occupancy (Figure 1A) per trimer. On the other hand, S protein and CVD432 showed a 1-RBD-up S protein with full ACE2 occupancy (~12%), a 2-RBD-up state with 2-ACE2 occupancy (~9%), all-RBD-down state, and other partial-to no-ACE2 occupancy 1-RBD- and 2-RBD-up states (Figure 1B). Overall similar conformational heterogeneity observed with either of our engineered ACE2 receptor traps suggests that ACE2 receptor traps do not fundamentally remodel the landscape of RBD-up vs RBD-down states. Although the fact that we observe slightly more of the "two-RBD-up" state with the CVD432 is consistent with its tighter binding affinity (as RBD cannot bind to ACE2 in its down conformation) we cannot rule out effects of differences in the CVD linker lengths or cryo-EM grid preparation on this equilibrium.

While ACE2 residues 18–614 were well resolved and could be fitted into our cryo-EM maps of the complexes between S protein/ACE2 receptor traps, we could not model the highly flexible collectrin domain of the ACE2 traps (residues 615–740) as well as the Fc-domains. Nevertheless, the WT-RBD/ACE2 receptor trap sub-region could be resolved at low to medium resolution. Local refinement of CVD293 or CVD432 (residues 18–614) with WT-RBD (residues 330–541, Wuhan-hu-1 strain) generated maps of resolution ~3.8–4.8 Å and 3.4–3.8 Å, respectively, for the interface residues (Figures 2A and S2–S5). As described above, the high level of heterogeneity between the 1-RBD-up and 2-RBD-up states for S protein with either CVD293 or CVD432 made obtaining high-resolution maps of the interface residues challenging. Continuous protein motions within the 1-RBD-up or 2-RBD-up states can be visualized by 3D variability analyses (3DVA)[17] (Figures S1A–S1C). Both S protein/CVD293 and S protein/CVD432 complexes showed considerable rotation relative to the vertical axis (~5-7°) in the 1-RBD-up/ACE2 bound sub-region of the cryo-EM map (Figures S1A and S1B). In contrast, the 2-RBD-up state of S protein/CVD432 showed lateral shift of the ACE2 bound RBD sub-region of the cryo-EM map relative to the vertical axis of rotation (Figure S1C). This high degree of variability in the ACE2 bound/RBD sub-region of the cryo-EM map further impeded high-resolution structure determination of the interface residues. Consequently, the precise rotamer positions, especially of key interface residues for CVD293 (engineered mutations - K31F, H34L, E35Q) or CVD432 (engineered mutations - K31F, N33D, H34S, E35Q) could not be obtained with high confidence directly from the cryo-EM maps. (Figures 2B and 2C; cryo-EM consensus models are shown fit to the cryo-EM maps).

Improving confidence of the interface interactions in limited resolution cryo-EM maps through Rosetta enabled multi-model workflow

Inspired by a previous ensemble model refinement approach to improve confidence in maps with resolution variation,[14] we
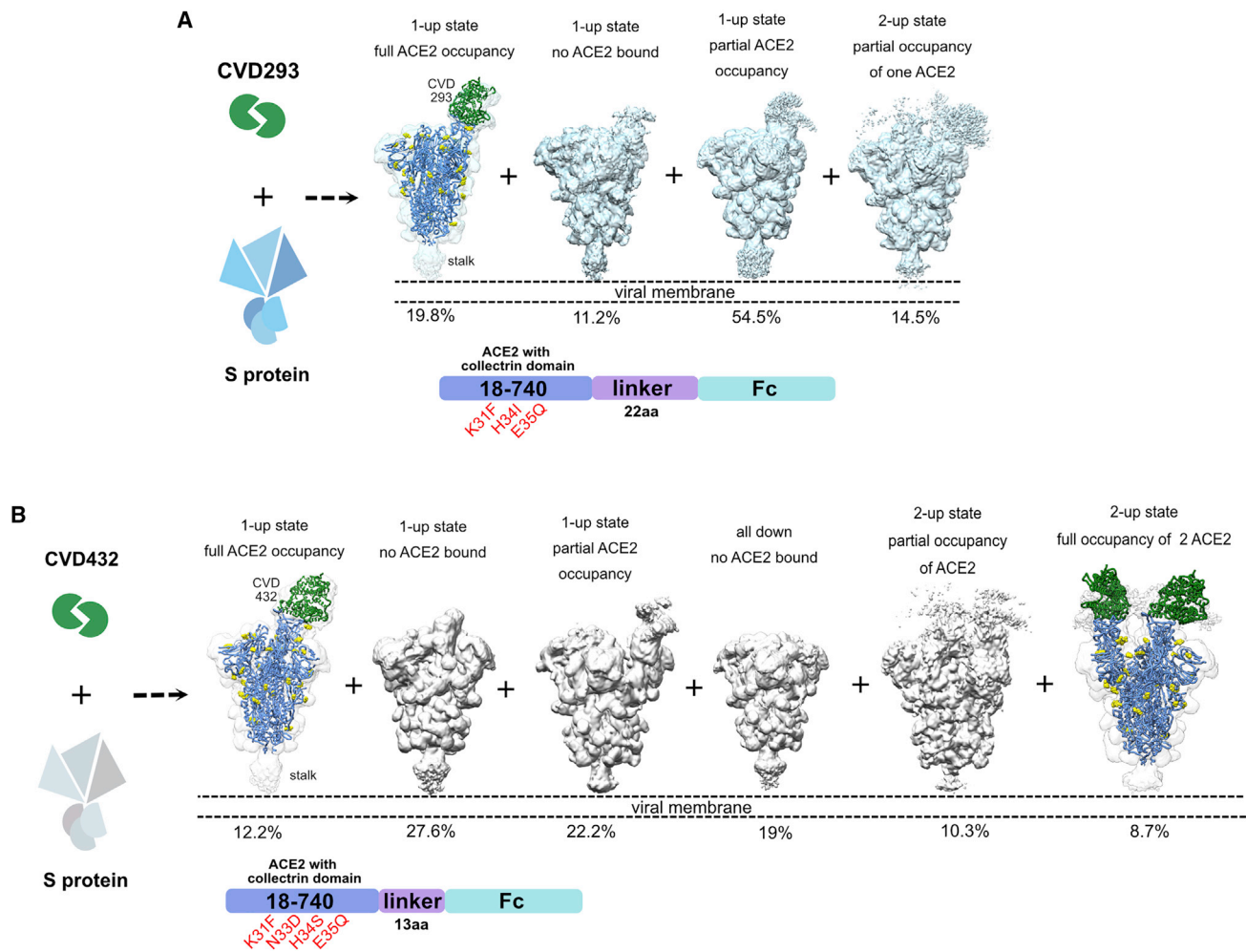
Figure 1. Cryo-EM reconstruction of the S protein with computationally designed, CVD293 or linker variant of the affinity-matured variant, CVD432

(A and B) Cryo-EM reconstructions of the S protein with CVD293 or CVD432 showing the heterogeneity in distribution of all RBD-down, 1-RBD- or 2-RBD-up states and variable ACE2 occupancy. Also shown is schematic of the primary structure of CVD293 or CVD432 and the engineered mutations, colored by domain. S protein is shown in blue and ACE2 is shown in green fitted into 1-RBD- or 2-RBD-up states. Partial glycosylation could be resolved in our structures and glycans are shown as yellow spheres.

See also Figures S1–S5 and Table S3.

developed a multi-model workflow that allowed for calculation of an "average predicted interface energy" metric across an ensemble of models consistent with the cryo-EM map in addition to the previously reported "average RMSD" metric. Together, these metrics provided a statistics-based view of the ACE2/RBD interface (Figure 3A). Briefly, 10-residue overlapping stretches of the ACE2 interface helix (residues 21–52) of each cryo-EM consensus model (WT-RBD [330–541]/ CVD293 [18–614] or WT-RBD [330–541]/CVD432 [18–614]) were subjected to a CartesianSampler mover within Rosetta that samples similar sequence and secondary structure fragments from within PDB and locally minimizes them into the cryo-EM map, generating 2,000 models for each 10-residue stretch. Each model was then all-atom minimized within the cryo-EM map using FastRelax mover with a scoring term for the model agreement with the cryo-EM map, as previously

described.[18] The Rosetta parameters and scoring functions used were based on the estimated map resolution.[19] This refinement protocol was iteratively run to generate a total of ~8,000 overlapping atomic models of the interface helix.

We next ranked the atomic models based on total Rosetta scores ensuring good geometries (pick top 200) and fits to the cryo-EM map (pick top 20 out of the above 200) for each 10-residue stretch to select a total of 80 models for the entire interface helix. The average per-residue side-chain RMSDs and predicted average interface energy for all the residues of the interface helix for the top-selected cryo-EM based models were then calculated (Figure 3B). We compared average per-residue side-chain RMSDs as we expected very small changes in the average backbone RMSDs, which can cause side-chain discrepancies being down-weighted in average full-residue RMSDs. We superimposed the interface
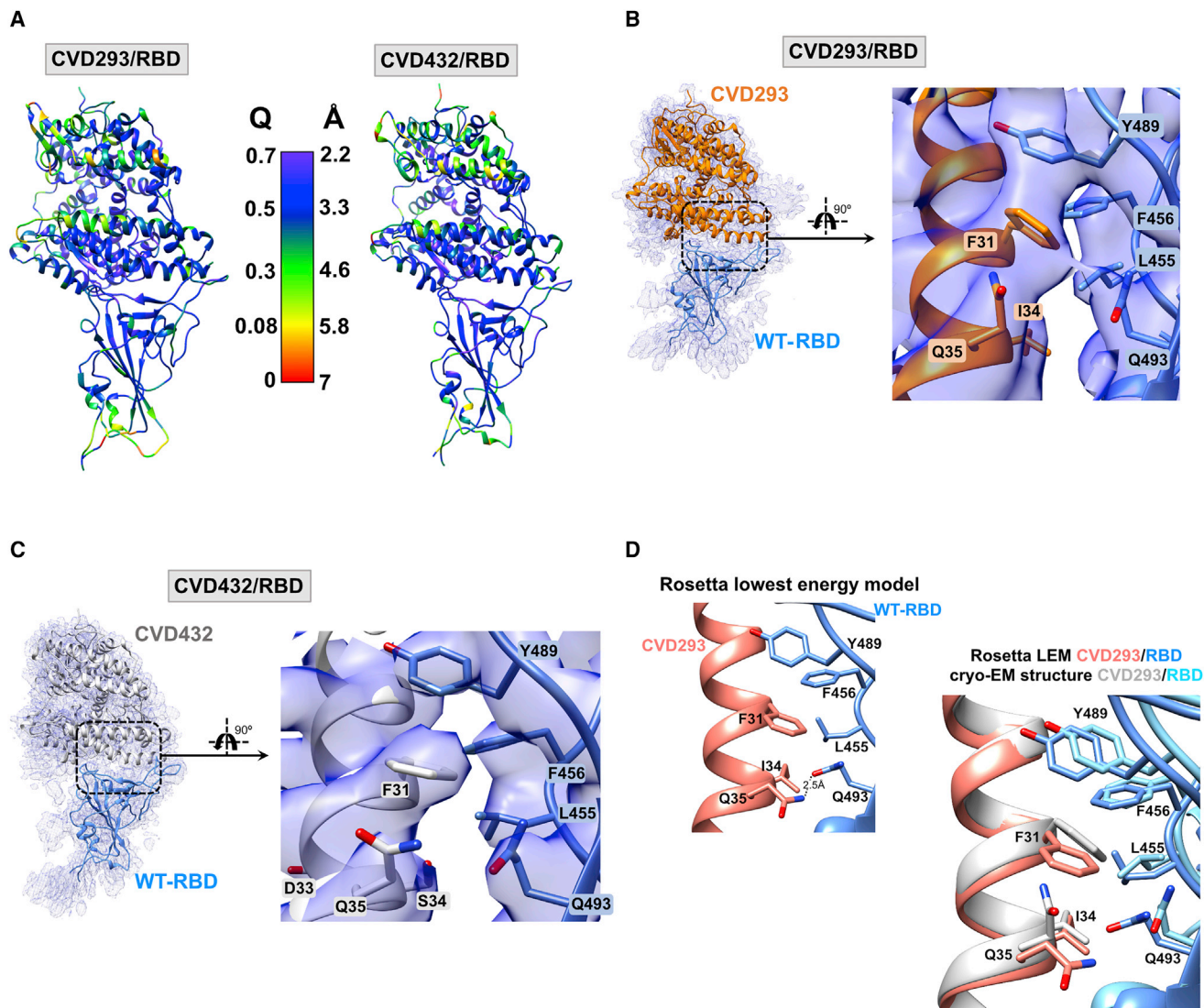
Figure 2. Cryo-EM reconstruction of WT-Spike-RBD with engineered ACE2 Fc-fusions reveal contributions from hydrophobic interactions at RBD-ACE2 interface

(A) WT-Spike-RBD/CVD293 and WT-Spike-RBD/CVD432 models colored by estimated per-residue Q-score ranging from 0 (red) to 0.7 (purple). The color bar shows corresponding estimated resolution in Å for each Q-score. Expected Q-score for 3.5 Å map is 0.49 and expected Q-score for 3.36 Å map is 0.52.

(B and C) Cryo-EM reconstructions of WT-Spike-RBD with either CVD293 or CVD432 show favorable π–π stacking interactions between WT-Spike-RBD residue Y489 and engineered ACE2 residue F31. In addition, there are also hydrophobic interactions between WT-Spike-RBD residue L455 and CVD293 residue I34. Hydrogen bond interactions between WT-Spike-RBD residue Q493 and CVD293 or CVD432 residue Q35 are not apparent in the cryo-EM consensus model.

(D) The Rosetta lowest energy model for CVD293 is overlaid with the cryo-EM model. Both models show hydrophobic and hydrogen bond interactions between CVD293 and WT-Spike-RBD residues that contribute to improved interface energy (REU) compared with the ACE2-WT-Spike-RBD interaction.

See also Figures S1–S5 and Table S3.

helix residues (residues 21–52) of the top 80 selected cryo-EM-based models for both CVD293 and CVD432 to analyze the convergence of the side-chain conformations and the intermolecular interaction with corresponding WT-RBD residues. We observed that while the interface residues of CVD293 (F31, I34) or CVD432 (F31) with low average side-chain RMSD make well-defined hydrophobic interactions with corresponding residues in WT-RBD (L455, F456, Y489), the high average side-chain RMSD residue (Q35 of both CVD293 and CVD432) makes hydrogen bond interactions

with neighboring WT-RBD residue (Q493) in over 90% of the atomic models (Figures 3C and 3D). We further noted that CVD432 high average side-chain RMSD residue, S34, can make both inter- (with WT-RBD residue Y453) and intra-molecular hydrogen bonds (with backbone carbonyl atoms of residues D30 or F31). We infer that the low average side-chain RMSD engineered hydrophobic residues of the ACE2 receptor traps likely provide the key functional interactions responsible for the improved binding affinity of the engineered receptor traps for WT-RBD.
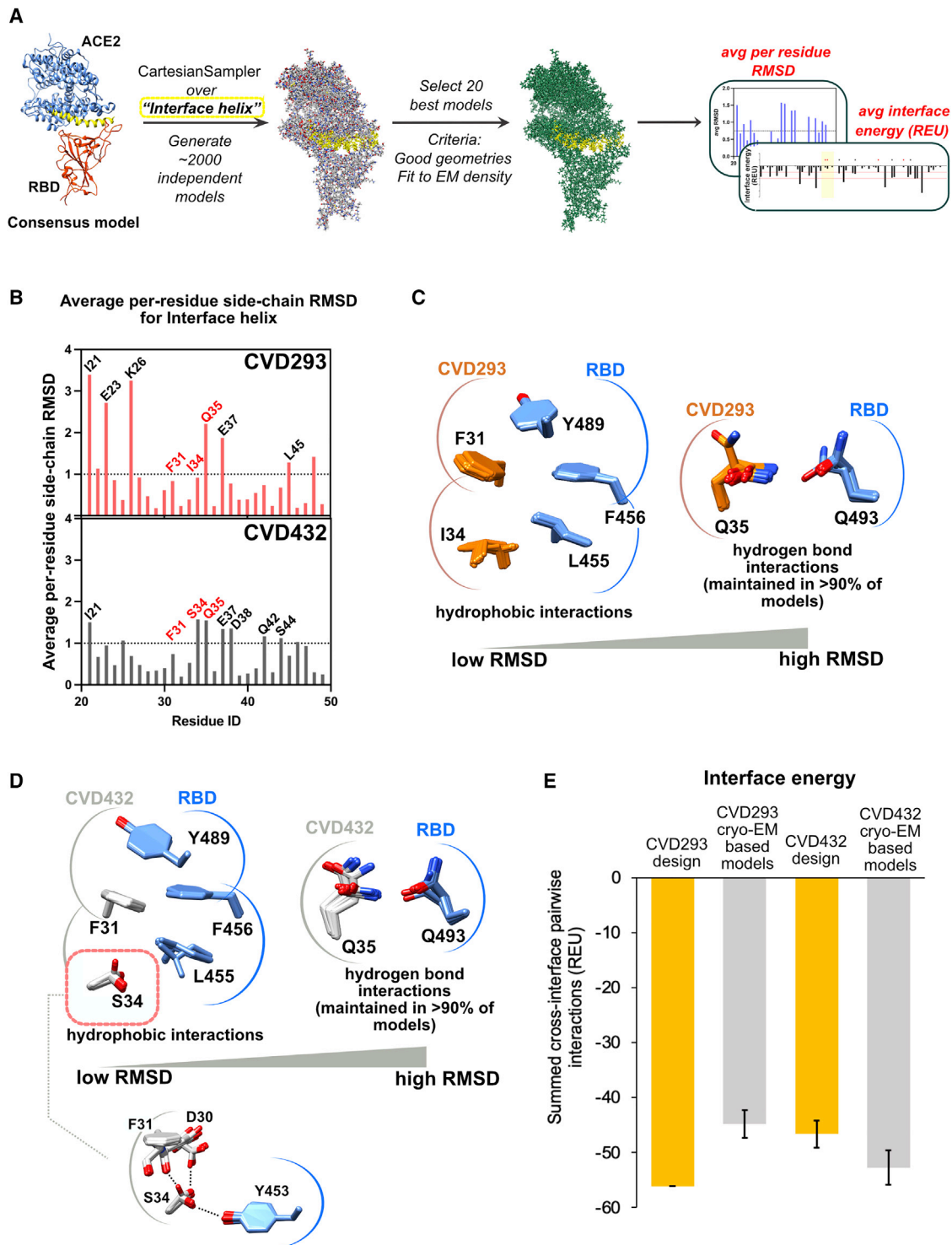
Figure 3. Multi-model pipeline improves confidence of molecular interactions at the interface residues in cryo-EM derived models of WT-Spike-RBD with engineered ACE2 Fc-fusions

(A) Multi-model pipeline with average Rosetta interface energy and average per-residue side-chain RMSD metrics for interface residue rotamer positions.

(B) Average per-residue side-chain RMSD for interface helix residues of CVD293 and CVD432.

(C and D) Superposition of critical interface residues of the top 80 selected cryo-EM based models for CVD293 and CVD432.

(E) Average Rosetta interface energy for CVD293 design model, CVD293 cryo-EM based models, CVD432 design model, and CVD432 cryo-EM based models. Error bars show SD calculated from 80 cryo-EM models or 80 design models.

See also Figures S6 and S7.

Analysis of the cryo-EM based models of CVD293 (18–614) and CVD432 (18–614) in complex with the WT-RBD (330–541)

The comparison between the original computationally designed model of the CVD293/WT-RBD complex and the cryo-EM-based models of the complex determined with our multi-model workflow revealed high overall structural agreement (Figure 2D). The all average Cα-RMSD between the computationally designed model and the experimentally solved cryo-EM consensus model of CVD293 (residues 18–614) was 0.93 Å, and the average Cα-RMSD for the interface helix (ACE2 residues 21–88, 322–329, 352–358, and Spike residues 444–446, 475–505) was 0.41 Å.

We next compared the calculated interface energy for the CVD293/WT-RBD interface in the designed model and the cryo-EM based models. We found that the predicted interface energy is considerably lower for the CVD293 design model (−58 REU) than the average of 80 CVD293 cryo-EM based models (−45 REU) (Figure 3E). This discrepancy between the predicted interface energy for the design model and the average interface energy calculated from the 80 cryo-EM based models is likely due to several differences in side-chain-mediated interactions involving designed residues. For example, isoleucine 34, a designed residue in CVD293, is predicted to contribute less to the interface energy in the cryo-EM based models (average from 80 atomic models of CVD293: −2.5 REU) than in the designed model (−3 REU), despite strong agreement in the atomic coordinates for this residue across all cryo-EM based models (Figure 2D). The predicted interaction energy of I34 is worse in the cryo-EM models than the designed model because its interaction partner across the interface, residue L455 of WT-RBD, universally adopts a different rotamer than the one in the original design model (Figure S7A).

Residue Q35, another designed residue in CVD293, showed the largest observed average per-residue side-chain RMSD among the designed positions on ACE2 in the cryo-EM-based models (Figure 3B). Although the Q35 side-chain often occupies a different rotamer in the cryo-EM-based models than in our original designed model of CVD293, it still makes a hydrogen bond with the WT-RBD residue Q493 as intended (Figure 3C). The WT-RBD residue Q493 shows minimal conformational heterogeneity across the 80 cryo-EM based models of the complex CVD293/WT-RBD, and it makes intra-molecular hydrogen bonds with the carbonyl group of the WT-RBD residue F490 to maintain the same loop conformation as seen in the complex between WT-ACE2 and WT-RBD (Figure S7A). It is plausible that the minimal average side-chain RMSD of residue Q493 and the overall similar loop conformation around residues F490-Q493 in the complex CVD293/WT-RBD contribute to the observed conserved hydrogen bond with residue Q35.

Another WT-ACE2 residue, K31, was mutated to a phenylalanine in CVD293. Consequently, the hydrogen bond between the WT-ACE2 residue K31 and the WT-RBD residue Q493 was lost in the complex CVD293/WT-RBD. Instead of making this hydrogen bond, the designed residue F31 in CVD293, with less than 1 Å average observed average side-chain RMSD, makes good packing interactions with other aromatics at the WT-RBD/engineered ACE2 trap interface as expected (Figure 3C). Overall, the all average Cα-RMSD between the computationally designed model and the experimentally solved cryo-EM consensus

model of CVD293 (residues 18–614) is close to 1 Å. However, using the cryo-EM-based models of complex CVD293/WT-RBD determined with our multi-model workflow, specific residue-pair interactions that were critical to improving the WT-ACE2/WT-RBD interface with our computational design strategy are revealed.

We next wanted to understand why the affinity maturation of CVD293 in our yeast surface display campaign resulted in the I34S interface mutation in the construct CVD432, which has improved binding affinity for WT-RBD. We first generated a CVD432 "design" model by mutating the residue I34 in the CVD293 cryo-EM consensus model to a serine *in silico*. We also made an N33D mutation to CVD293 *in silico* even though this position is outside the RBD binding interface, because this mutation was also identified by yeast surface display in CVD432. The calculated interface energy for the CVD432 designed model/WT-RBD interface is higher (−47 REU) than the average interface energy from 80 cryo-EM-based models of the complex CVD432/WT-RBD (−53 REU) (Figure 3E). It can be inferred that simple *in silico* mutations do not provide a full explanation for the improved binding affinity between the engineered ACE2 trap and the WT-RBD, highlighting the value of the cryo-EM structure solution.

Comparing the cryo-EM-based models of the complexes CVD293/WT-RBD and CVD432/WT-RBD, we find that the calculated interface energy from the average of 80 cryo-EM-based models of the complex CVD432/WT-RBD is lower (−53 REU) than the average of 80 cryo-EM-based models of the complex CVD293/WT-RBD (−45 REU) (Figure 3E). The decrease in calculated interface energy for the cryo-EM-based models of the complex CVD432/WT-RBD as compared with that of the complex CVD293/WT-RBD is surprising for three reasons. First, S34 can adopt several different conformations (Figure 3D). Second, S34 makes weaker energetic contributions to the interface energy in all of the cryo-EM-based models of the complex CVD432/WT-RBD than I34 in the complex CVD293/WT-RBD, regardless of the serine rotamer (Figure S6A). Third, S34 in CVD432 also has a higher average per-residue energy than I34 in CVD293 (Figure S6B). It is possible that a serine was enriched at position 34 in our directed evolution campaign using error-prone PCR because of the isoleucine parental codon, from which single base mutations could only lead to large hydrophobic amino acids, serine, threonine, or asparagine. Of these possibilities, serine is the smallest amino acid, and might have been favored simply to allow the other ACE2 residues to maintain favorable interactions with the RBD.

It appears that no individual residue is fully responsible for the improved interface energy in CVD432 cryo-EM-based models; rather, this improvement is the sum of several small improvements among many residues at the interface (Figure S6A). The enhanced affinity in CVD432 cryo-EM-based models may also be an indirect effect of a lower average side-chain RMSD for the interface residues and overall stabilization of the interface helix by the CVD432 mutations. This CVD432-specific stabilization could result from a main-chain-side-chain hydrogen bond between the S34 hydroxyl group and the F31 backbone carbonyl group in ACE2 (Figure 3D) that is not appropriately scored by Rosetta, and from the lower average per-residue energies for residues in the ACE2 interface helix that do not interact with the

Figure 4. Binding to Omicron- and Delta-RBD and neutralization of Omicron- and Delta-SARS-CoV-2 VOCs by CVD293 and CVD432

(A and B) Left panel: Predictions based on Rosetta interface energy calculations suggest that Omicron-RBD binds CVD293 and CVD432 with high affinity. Residue-pair interactions of RBD residues with CVD293/CVD432 residue F31 (yellow), with residue I34/S34 (blue) and with residue Q35 (red) are shown. Right panel: Zoomed-in view of the interface of the models Omicron-RBD/CVD293 and Omicron-RBD/CVD432. Wheat-colored residues indicate RBD interactions ACE2 K/F31. Blue residues indicate RBD interactions with ACE2 H/I/S34. Magenta residues indicate RBD interactions with more than one engineered ACE2 residue.

(C) Biolayer interferometry measurements for CVD293 or CVD432 interactions with Omicron- or Delta-RBD.

(D) CVD293 and CVD432 potently neutralize vesicular stomatitis virus (VSV) pseudotyped with SARS-CoV2 Omicron- and Delta-Spike. Error bars represent SD over all technical replicates from two biological replicates.

See also Figures S8 and S9, Tables S1, S2, and S4.

ACE2 receptor traps bind Omicron-RBD with increased affinity and neutralize the SARS-CoV-2 VOC

Several of the 37 Omicron-Spike mutations have been observed in other SARS-CoV-2 variants. For example, previous reports suggest that the N501Y mutation increases WT-ACE2 binding affinity while the K417N mutation decreases the WT-ACE2 binding affinity in some SARS-CoV-2 variants.[22–27] Fourteen of the 37 mutations have not been reported previously in other variants but together were reported to improve the binding affinity ~2- to 3-fold between Omicron-RBD and WT-ACE2.[3,4,28] For example, while the Y505H mutation leads to loss in hydrogen bond interactions with WT-ACE2 residue E37, there are several compensatory mutations in the Omicron-RBD. These include Q493R and G496S, which result in new hydrogen bonds with WT-ACE2 residues E35 and K353, respectively and several others (Table S1, residue pairs colored green).

Our ACE2 receptor traps have >170-fold improved binding affinity for monomeric WT-RBD compared with the binding affinity of WT-ACE2 for WT-RBD.[13] To evaluate if our ACE2 receptor traps would bind Omicron-RBD, we first generated models of Omicron-RBD (330–530)/CVD293 (18–614) and Omicron-RBD (330–530)/CVD432 (18–614) by superimposing and replacing WT-RBD in our respective cryo-EM local refinement of the complexes with Omicron-RBD from the recently determined cryo-EM structure of Omicron-Spike (330–530)/WT-ACE2 (19–613) (PDB ID: 7T9L, EMD: 25761) (Figures 4A and 4B; panels on the right) and minimizing the complexes. Next, we calculated the Rosetta

RBD, particularly at position 33 (an asparagine in CVD293, but mutated to an aspartic acid in CVD432) (Figure S6C). Interestingly, in all our models, N33D mutation breaks a hydrogen bond with the Q96 side-chain within ACE2 yielding a subtle shift of the neighboring residues toward the RBD (Figure S7B). This is correlated with subtly lower interface energies for these residues and lower total energy for D33 (Figures S6B and S6C). The N33D mutation was also observed to improve the RBD binding interaction in another ACE2 engineering study[20] and a computational analysis of ACE2 mutations.[21] Altogether, the improved SARS-CoV-2 neutralization by CVD432 compared with CVD293 is driven by mutations at the interface that improve binding in addition to stability-enhancing mutations outside the interface. As such, both protein stability and interface pre-organization contribute to the overall stability of the receptor trap-RBD complex.

interface energies of these models (Figures 4A and 4B; panels on the left). Although we predict an energy penalty for engineered interface interaction residue pairs going from R493/E35 in Omicron-RBD/WT-ACE2 to R493/Q35 in Omicron-RBD/CVD293 or Omicron-RBD/CVD432 (in red in Figures 4A and 4B; panels on the left), overall, we also predict improved binding affinities between the Omicron-RBD and the engineered ACE2 receptor traps. Total interface energy for the interface residue pairs contributing to the affinity between CVD293 or CVD432 to Omicron-RBD was calculated to be −10.77 REU and −8.5 REU, respectively. For reference, the total interface energy for the interface residue pairs contributing to the affinity between WT-ACE2 and Omicron-RBD was calculated to be −4.99 REU. Potential contributions from interaction residue pairs L455/F31, Y489/F31, and F31/R493 (in yellow in Figures 4A and 4B; panels on the left) and other residue-pair interactions between residue I34 of CVD293 or S34 of CVD432 and L455 of Omicron-RBD may be improving the interface affinity (in blue in Figures 4A and 4B; panels on the left).

To test whether improved predicted interface energies correspond to increased apparent binding affinities, we assayed the binding affinity of CVD293 and CVD432 for Omicron-RBD by performing biolayer interferometry (BLI). The BLI-determined dissociation constant (K_D) between Omicron-RBD/CVD293 (K_D = 4.2 nM) or Omicron-RBD/CVD432 (K_D = 0.53 nM) was measured to be 10- and 100-fold lower than that for Omicron-RBD/WT-ACE2(18–740)-Fc-fusion, respectively (Figures 4C, S9, and Table S2). The hydrophobic interactions specific to Omicron-RBD/ACE2 receptor trap complexes, along with the several compensatory mutations in Omicron-RBD/ACE2 interface that are also maintained with the ACE2 receptor traps, likely result in the BLI-measured improved affinity. Interestingly, CVD293 and CVD432 showed similar (K_D = 1.9 nM) or about 100-fold (K_D = 0.071 nM) lower K_D for Delta-RBD, respectively.

Finally, to determine whether the improved in vitro binding affinity also leads to higher potency in viral neutralization, we tested the neutralization of Omicron (BA.1) and Delta (B.1.617.2) SARS-CoV-2 variants by our ACE2 receptor traps in pseudoviruses bearing these variants of interest generated using recombinant vesicular stomatitis virus (VSV) expressing green fluorescent protein (GFP) in place of the VSV glycoprotein (rVSV ΔG-GFP). We compared the neutralization of Delta and Omicron pseudoviruses to a control Spike-WT pseudovirus with a D614G mutation. The pseudovirus neutralization assays demonstrated that both CVD293 and CVD432 neutralize Delta (half maximal inhibitory concentration [IC50] = 1.4 nM, 1.6 nM, respectively) and Omicron (IC50 = ND, 0.15nM, respectively) pseudoviruses, with IC50 values improved between 2- and 20-fold over Spike-WT (IC50 = 2.6 nM, 3.7 nM, respectively) pseudovirus (Figure 4D). Taken together, the results from the BLI and pseudovirus neutralization assays suggest that our engineered ACE2 traps, although computationally designed and affinity improved against WT-RBD, can still bind the rapidly evolving SARS-CoV-2 variants with high affinity and potently block virus entry into cells.

DISCUSSION

Over the course of the current pandemic, several neutralizing monoclonal antibodies (mAbs) have been identified and some

have been evaluated clinically as therapeutic candidates against SARS-CoV-2 infection.[29–37] These mAbs are broadly categorized based on their ability to bind RBD in the "up" or "down" conformations on Spike ectodomain, engaging epitopes that can or cannot block ACE2 receptor binding to the RBD.[31,37–40] Several of the mAbs that bind the ACE2 recognition site (also called the receptor-binding motif, RBM) within the RBD lost in vitro neutralization activity against the Omicron-VOC.[3,4,41] Interestingly, only the S2K146 mAb that binds SARS-CoV-2, SARS-CoV and other sarbecoviruses through ACE2 molecular mimicry retained neutralization activity against the Omicron-VOC.[3,41] This suggests that ACE2 specific binding epitope residues have a higher barrier for emergence of escape mutants.

We[13] and others[13,20,42,43] have explored "ACE2 decoy receptors" or "ACE2 receptor traps" that bind and block the RBD and neutralize SARS-CoV-2 pseudovirus. Others have shown that ACE2-Fc-fusion proteins can neutralize live SARS-CoV-2 virus isolates from patients[44] and in live viral challenge models in vivo[45] providing further evidence that ACE2-Fc-fusion decoy receptors are viable alternative for SARS-CoV-2 virus neutralization. Our ACE2 receptor traps were computationally designed, and affinity matured against the WT-RBD and their SARS-CoV-2 virus neutralization ability improved as Fc-fusions. The cryo-EM structures of the ACE2 receptor traps with the S protein helped validate the mechanism of action for our computationally designed traps and determine the molecular basis for the additional binding affinity improvement by the affinity-matured traps. The in vivo efficacy of our Fc-fusion ACE2 receptor traps may be further enhanced due to the Fc-effector functions such as antibody-dependent cellular cytotoxicity (ADCC), cellular phagocytosis (ADCP), and complement deposition (ADCD) as shown elegantly for other ACE2 Fc-fusions in a recent study.[46] We believe that by iterating on our computational design workflow with some changes one can obtain even tighter RBD interacting ACE2 variants. We would update the workflow by (1) computationally designing our model ensembles instead of a single model, and also by (2) evaluating the stability of ACE2 alone in addition to the ACE2-RBD complex. We reason that during this process it would be beneficial to catalog the most crucial interactions between the various ACE2 and RBD mutants in future designs to maintain broad neutralization efficacy, and it is possible that introducing an affinity-enhancing mutation in an ACE2 trap for improved interactions with a predicted RBD mutant could abolish binding to a different RBD mutant. However, because of the large, broad-binding interface between the RBD and the ACE2, it is unlikely that the loss of one or two important interactions will completely ablate the interaction and neutralization, especially because any mutant virus will still require ACE2 binding to enter the cell.

From the cryo-EM structures and the derived multi-model workflow, we learned key lessons for designing strong binders: that distributed binding interactions across a protein-protein interface are more effective as compared with reliance on one or two important cross-interface interactions; and that it is important to prioritize the stability of all proteins individually in addition to the protein complex. Importantly, such stability may come from substitutions away from directly interacting residues, like N33D mutation in CVD432 that yields a lower energy conformation for that residue allowing for lower interface energies of surrounding residues. The data suggest that the stability and pre-organization of each protein

at the interface is as important as the cross-interface interactions in the overall stability of the complex. We believe our multi-model analysis is a useful departure from the way current cryo-EM-based structural interfaces are analyzed, especially for structures that are worse than 4 Å resolution and can be used to analyze protein-protein interfaces in other systems. Building on the multi-model workflow developed for evaluation of cryo-EM structures,[14] we calculated the Rosetta interaction energies for the top model ensemble instead of one best-built consensus model. This analysis incorporates the uncertainties in placement of some unresolved side chains directly into the interface energy calculations leading to more robust understanding of the interface. However, we would like to note certain limitations of the presented multi-model cryo-EM approach for prediction of the strength of protein-protein interactions. Specifically, correct interpretation of inter-residue interaction energies in the model ensemble relies on exhaustive conformational sampling. In cases such as presented here, where the cryo-EM map resolution is of 3.3–3.5 Å, it is likely to be not a concern as the constraints of the experimental cryo-EM map significantly reduce the number of possible consistent protein models. However, at lower experimental map resolutions such exhaustive sampling is likely to be computationally limited, preventing accurate interpretation of interface interactions. In these cases significantly more extensive sampling with Rosetta will be required or use of orthogonal molecular dynamics-based approaches may be beneficial, such as Cryo-Fold.[47]

Recently, two engineered ACE2 decoy receptors have been reported to broadly neutralize SARS-CoV-2 variants including the Omicron-VOC.[48,49] These engineered decoy receptors neutralized the Omicron-VOC with IC50s comparable or even better than Omicron-VOC neutralizing mAbs such as VIR-7831. Apeiron's APN01, a WT ACE2 soluble extracellular domain, has also shown promising results in early-phase clinical trials and retains the ability to neutralize multiple VOCs.[50] Furthermore, in a laboratory simulation of viral mutation under neutralizing selective pressure, another engineered ACE2 decoy receptor, 3n39v2 retained its neutralizing capacity over several passage cycles.[43] Thus, soluble engineered ACE2 receptors have therapeutic value against SARS-CoV-2 variants and may continue to be relevant as this virus evolves further.

Application of the multi-model workflow increased our confidence in the atomic positions of computationally designed amino acids at the ACE2-Spike interface. This laid the groundwork for further improvements in the receptor trap design and allowed us to model interactions of the receptor traps with the Omicron-RBD. We experimentally verified the Omicron-RBD binding interactions with the receptor traps using BLI and pseudovirus neutralization assays, demonstrating that our ACE2 receptor traps designed for neutralization of S protein from SARS-CoV-2 remain robust to dozens of mutations in the VOCs. This is both surprising and exciting since our computational design and affinity maturation optimized the binding interface of ACE2 to selectively bind the targeted antigen, WT-RBD. These results are also in contrast to pan-specific antibodies that are affinity matured to be highly epitope- or antigen-specific binders.[51–53] Perhaps, the particular hydrophobic mutations at the binding interface of our ACE2 receptor traps make them more adaptable to Spike-RBD mutations. Alternatively, as the virus evolves, its affinity for its entry receptor increases and fortuitously also to our ACE2 receptor traps.

In addition to the RBM antigenic site, other mAbs with antigenic sites outside the RBM such as Sotrovimab, S309, S2X259, and S2H97 also retained neutralization activity against Omicron-VOC.[3,4,28] A bifunctional antibody format called ReconnAbs (receptor-blocking conserved non-neutralizing antibodies) was recently shown to convert non-neutralizing antibodies to potent neutralizers of SARS-CoV-2 VOCs by linking the "WT-ACE2 receptor" to a bispecific antibody targeting two non-overlapping conserved epitopes.[54] We envision future versions of our ACE2-receptor trap binders to be knob-in-hole bispecifics and other Fc-fusion formats with one engineered ACE2 arm and other arm(s) as mAbs with antigenic sites outside the RBM, other non-neutralizing mAbs or Vh domains.

Overall, this study exemplifies how technical advances in cryo-EM and computational protein design methods can be combined toward improving the *design-build-test* cycle for engineering potent biotherapeutics, even for difficult targets such as the ACE2 complex with the SARS-CoV-2 Spike protein. Furthermore, this workflow can be generalized for solving the cryo-EM structures of other protein complexes and improving computational protein design protocols.

QCRG STRUCTURAL BIOLOGY CONSORTIUM

Cryo-EM grid freezing/collection team: *Axel F. Brilot, Gregory E. Merz, Alexandrea N. Rizo*, Caleigh M. Azumaya, Julian R. Braxton, Meghna Gupta, Fei Li, Kyle E. Lopez, Arthur Melo, Frank Moss, Joana Paulino, Thomas H. Pospiech Jr., Sergei Pourmal, Cristina Puchades, Amber M. Smith, Ming Sun, Paul V. Thomas, Feng Wang, and Zanlin Yu. **Cryo-EM data processing team:** *Axel F. Brilot, Gregory E. Merz, Alexandrea N. Rizo, Soumya G. Remesh*, Daniel Asarnow, Julian R. Braxton, Melody G. Campbell, Cynthia M. Chio, Un Seng Chio, Miles Sasha Dickinson, Devan Diwanji, Bryan Faust, Meghna Gupta, Nick Hoppe, Mingliang Jin, Fei Li, Junrui Li, Yanxin Liu, Henry C. Nguyen, Joana Paulino, Thomas H. Pospiech Jr., Sergei Pourmal, Smriti Sangwan, Raphael Trenker, Donovan Trinidad, Eric Tse, Kaihua Zhang, and Fengbo Zhou. **Mammalian cell expression team:** *Evelyn Hernandez, Devan Diwanji, Amber M. Smith,* Caleigh M. Azumaya, Christian Billesboelle, Alisa Bowen, Melody G. Campbell, Nick Hoppe, Yen-Li Li, Edmond Linossi, Jocelyne Lopez, Phuong Nguyen, Carlos Nowotny, Quynh Mai, Hevatib Mehmood, Michael Paul, Cristina Puchades, Mali Safari, Smriti Sangwan, Kaitlin Schaefer, Raphael Trenker, Tsz Kin Martin Tsui, Natalie Whitis, and Jianhua Zhao. **Protein purification team:** *Michelle Moritz, Sergei Pourmal*, Daniel Asarnow, Caleigh M. Azumaya, Cynthia M. Chio, Bryan Faust, Meghna Gupta, Raghav Kalia, Kate Kim, Tristan W. Owens, Joana Paulino, Komal Pawar, Jessica K. Peters, Kaitlin Schaefer, and Tsz Kin Martin Tsui. **Crystallography team:** *Nadia Herrera, Huong T. Kratochvil, Ursula Schulze-Gahmen, Iris D. Young*, Justin Biel, Ishan Deshpande, and Xi Liu. **Bacterial expression team:** *Amy Diallo, Meghna Gupta*, Jen Chen, Loan Doan, Sebastian Flores, Mingliang Jin, Huong T. Kratochvil, Victor L. Lam, Yang Li, Megan Lo, Gregory E. Merz, Joana Paulino, Aye C. Thwin, Erron W. Titus, Zanlin Yu, Fengbo Zhou, and Yang Zhang. **Infrastructure team:** David Bulkley, Arceli Joves, Almarie Joves, Liam McKay, Mariano Tabios, and Eric Tse. **Leadership team:** David A. Agard, Yifan Cheng, James S. Fraser, Adam Frost, Natalia Jura, Tanja

Kortemme, Nevan J. Krogan, Aashish Manglik, Oren S. Rosenberg, Daniel R. Southworth, Robert M. Stroud & Kliment A. Verba.

STAR★METHODS

Detailed methods are provided in the online version of this paper and include the following:

- KEY RESOURCES TABLE
- RESOURCE AVAILABILITY
  - Lead contact
  - Materials availability
  - Data and code availability
- EXPERIMENTAL MODEL AND SUBJECT DETAILS
  - Bacterial strains
  - Cell lines
- METHOD DETAILS
  - Cloning, expression and purification of protein constructs
  - High resolution "final consensus" model building
  - Multi-model pipeline
  - Energy calculations
  - Design models of the ACE2 domain of CVD432
  - Determination of binding affinity using biolayer interferometry (BLI)
  - Pseudovirus production
  - Pseudovirus neutralization assay
- QUANTIFICATION AND STATISTICAL DETAILS

SUPPLEMENTAL INFORMATION

Supplemental information can be found online at https://doi.org/10.1016/j.str.2023.01.009.

DECLARATION OF INTERESTS

The authors declare no competing interests.

REFERENCES

1. Walls, A.C., Park, Y.-J., Tortorici, M.A., Wall, A., McGuire, A.T., and Veesler, D. (2020). Structure, function, and antigenicity of the SARS-CoV-2 spike glycoprotein. Cell 181, 281–292.e6. https://doi.org/10.1016/j.cell.2020.02.058.

2. Viana, R., Moyo, S., Amoako, D.G., Tegally, H., Scheepers, C., Althaus, C.L., Anyaneji, U.J., Bester, P.A., Boni, M.F., Chand, M., et al. (2022). Rapid epidemic expansion of the SARS-CoV-2 Omicron variant in Southern Africa. Nature 603, 679–686. https://doi.org/10.1038/s41586-022-04411-y.

3. Cameroni, E., Bowen, J.E., Rosen, L.E., Saliba, C., Zepeda, S.K., Culap, K., Pinto, D., VanBlargan, L.A., De Marco, A., di Iulio, J., et al. (2022). Broadly neutralizing antibodies overcome SARS-CoV-2 Omicron antigenic shift. Nature 602, 664–670. https://doi.org/10.1038/s41586-021-04386-2.

4. Mannar, D., Saville, J.W., Zhu, X., Srivastava, S.S., Berezuk, A.M., Tuttle, K.S., Marquez, A.C., Sekirov, I., and Subramaniam, S. (2022). SARS-CoV-2 Omicron variant: antibody evasion and cryo-EM structure of spike protein-ACE2 complex. Science 375, 760–764. https://doi.org/10.1126/science.abn7760.

5. Cao, Y., Wang, J., Jian, F., Xiao, T., Song, W., Yisimayi, A., Huang, W., Li, Q., Wang, P., An, R., et al. (2022). Omicron escapes the majority of existing SARS-CoV-2 neutralizing antibodies. Nature 602, 657–663. https://doi.org/10.1038/s41586-021-04385-3.

6. Liu, L., Iketani, S., Guo, Y., Chan, J.F.-W., Wang, M., Liu, L., Luo, Y., Chu, H., Huang, Y., Nair, M.S., et al. (2022). Striking antibody evasion manifested by the Omicron variant of SARS-CoV-2. Nature 602, 676–681. https://doi.org/10.1038/s41586-021-04388-0.

7. Planas, D., Saunders, N., Maes, P., Guivel-Benhassine, F., Planchais, C., Buchrieser, J., Bolland, W.-H., Porrot, F., Staropoli, I., Lemoine, F., et al. (2022). Considerable escape of SARS-CoV-2 Omicron to antibody neutralization. Nature 602, 671–675. https://doi.org/10.1038/s41586-021-04389-z.

8. VanBlargan, L.A., Errico, J.M., Halfmann, P.J., Zost, S.J., Crowe, J.E., Purcell, L.A., Kawaoka, Y., Corti, D., Fremont, D.H., and Diamond, M.S. (2021). An infectious SARS-CoV-2 B.1.1.529 Omicron virus escapes neutralization by several therapeutic monoclonal antibodies. Preprint at bioRxiv. https://doi.org/10.1101/2021.12.15.472828.

9. Cele, S., Jackson, L., Khoury, D.S., Khan, K., Moyo-Gwete, T., Tegally, H., San, J.E., Cromer, D., Scheepers, C., Amoako, D., et al. (2021). SARS-CoV-2 Omicron has extensive but incomplete escape of Pfizer BNT162b2 elicited neutralization and requires ACE2 for infection. Preprint at medRxiv. https://doi.org/10.1101/2021.12.08.21267417.

10. Wilhelm, A., Widera, M., Grikscheit, K., Toptan, T., Schenk, B., Pallas, C., Metzler, M., Kohmer, N., Hoehl, S., Helfritz, F.A., et al. (2021). Reduced neutralization of SARS-CoV-2 omicron variant by vaccine sera and monoclonal antibodies. Preprint at medRxiv. https://doi.org/10.1101/2021.12.07.21267432.

11. McCallum, M., Walls, A.C., Sprouse, K.R., Bowen, J.E., Rosen, L.E., Dang, H.V., De Marco, A., Franko, N., Tilles, S.W., Logue, J., et al. (2021). Molecular basis of immune evasion by the Delta and Kappa SARS-CoV-2 variants. Science 374, 1621–1626. https://doi.org/10.1126/science.abl8506.

12. Mlcochova, P., Kemp, S.A., Dhar, M.S., Papa, G., Meng, B., Ferreira, I.A.T.M., Datir, R., Collier, D.A., Albecka, A., Singh, S., et al. (2021). SARS-CoV-2 B.1.617.2 Delta variant replication and immune evasion. Nature 599, 114–119. https://doi.org/10.1038/s41586-021-03944-y.

13. Glasgow, A., Glasgow, J., Limonta, D., Solomon, P., Lui, I., Zhang, Y., Nix, M.A., Rettko, N.J., Zha, S., Yamin, R., et al. (2020). Engineered ACE2 receptor traps potently neutralize SARS-CoV-2. Proc. Natl. Acad. Sci. USA 117, 28046–28055. https://doi.org/10.1073/pnas.2016093117.

14. Herzik, M.A., Fraser, J.S., and Lander, G.C. (2019). A multi-model approach to assessing local and global cryo-EM map quality. Structure 27, 344–358.e3. https://doi.org/10.1016/j.str.2018.10.003.

15. Zhou, T., Tsybovsky, Y., Gorman, J., Rapp, M., Cerutti, G., Chuang, G.-Y., Katsamba, P.S., Sampson, J.M., Schön, A., Bimela, J., et al. (2020). Cryo-EM structures of SARS-CoV-2 spike without and with ACE2 reveal a pH-dependent switch to mediate endosomal positioning of receptor-binding domains. Cell Host Microbe 28, 867–879.e5. https://doi.org/10.1016/j.chom.2020.11.004.

16. Yan, R., Zhang, Y., Li, Y., Ye, F., Guo, Y., Xia, L., Zhong, X., Chi, X., and Zhou, Q. (2021). Structural basis for the different states of the spike protein of SARS-CoV-2 in complex with ACE2. Cell Res. 31, 717–719. https://doi.org/10.1038/s41422-021-00490-0.

17. Punjani, A., and Fleet, D.J. (2021). 3D variability analysis: resolving continuous flexibility and discrete heterogeneity from single particle cryo-EM. J. Struct. Biol. 213, 107702. https://doi.org/10.1016/j.jsb.2021.107702.

18. DiMaio, F., Song, Y., Li, X., Brunner, M.J., Xu, C., Conticello, V., Egelman, E., Marlovits, T., Cheng, Y., and Baker, D. (2015). Atomic-accuracy models from 4.5-Å cryo-electron microscopy data with density-guided iterative local refinement. Nat. Methods 12, 361–365. https://doi.org/10.1038/nmeth.3286.

19. Wang, R.Y.-R., Song, Y., Barad, B.A., Cheng, Y., Fraser, J.S., and DiMaio, F. (2016). Automated structure refinement of macromolecular assemblies from cryo-EM maps using Rosetta. Elife 5, e17219. https://doi.org/10.7554/eLife.17219.

20. Chan, K.K., Dorosky, D., Sharma, P., Abbasi, S.A., Dye, J.M., Kranz, D.M., Herbert, A.S., and Procko, E. (2020). Engineering human ACE2 to optimize binding to the spike protein of SARS coronavirus 2. Science 369, 1261–1265. https://doi.org/10.1126/science.abc0870.

21. Chowdhury, R., Boorla, V.S., and Maranas, C.D. (2020). Computational biophysical characterization of the SARS-CoV-2 spike protein binding with the ACE2 receptor and implications for infectivity. Comput. Struct. Biotechnol. J. 18, 2573–2582. https://doi.org/10.1016/j.csbj.2020.09.019.

22. Zhu, X., Mannar, D., Srivastava, S.S., Berezuk, A.M., Demers, J.-P., Saville, J.W., Leopold, K., Li, W., Dimitrov, D.S., Tuttle, K.S., et al. (2021). Cryo-electron microscopy structures of the N501Y SARS-CoV-2 spike protein in complex with ACE2 and 2 potent neutralizing antibodies. PLoS Biol. 19, e3001237. https://doi.org/10.1371/journal.pbio.3001237.

23. Mannar, D., Saville, J.W., Zhu, X., Srivastava, S.S., Berezuk, A.M., Zhou, S., Tuttle, K.S., Kim, A., Li, W., Dimitrov, D.S., et al. (2021). Structural analysis of receptor binding domain mutations in SARS-CoV-2 variants of concern that modulate ACE2 and antibody binding. Cell Rep. 37, 110156. https://doi.org/10.1016/j.celrep.2021.110156.

24. Barton, M.I., MacGowan, S.A., Kutuzov, M.A., Dushek, O., Barton, G.J., and van der Merwe, P.A. (2021). Effects of common mutations in the SARS-CoV-2 Spike RBD and its ligand, the human ACE2 receptor on binding affinity and kinetics. Elife 10, e70658. https://doi.org/10.7554/eLife.70658.

25. Liu, H., Zhang, Q., Wei, P., Chen, Z., Aviszus, K., Yang, J., Downing, W., Jiang, C., Liang, B., Reynoso, L., et al. (2021). The basis of a more contagious 501Y.V1 variant of SARS-CoV-2. Cell Res. 31, 720–722. https://doi.org/10.1038/s41422-021-00496-8.

26. Tian, F., Tong, B., Sun, L., Shi, S., Zheng, B., Wang, Z., Dong, X., and Zheng, P. (2021). N501Y mutation of spike protein in SARS-CoV-2 strengthens its binding to receptor ACE2. Elife 10, e69091. https://doi.org/10.7554/eLife.69091.

27. Laffeber, C., de Koning, K., Kanaar, R., and Lebbink, J.H.G. (2021). Experimental evidence for enhanced receptor binding by rapidly spreading SARS-CoV-2 variants. J. Mol. Biol. 433, 167058. https://doi.org/10.1016/j.jmb.2021.167058.

28. McCallum, M., Czudnochowski, N., Rosen, L.E., Zepeda, S.K., Bowen, J.E., Walls, A.C., Hauser, K., Joshi, A., Stewart, C., Dillen, J.R., et al. (2022). Structural basis of SARS-CoV-2 Omicron immune evasion and receptor engagement. Science 375, 864–868. https://doi.org/10.1126/science.abn8652.

29. Baum, A., Fulton, B.O., Wloga, E., Copin, R., Pascal, K.E., Russo, V., Giordano, S., Lanza, K., Negron, N., Ni, M., et al. (2020). Antibody cocktail to SARS-CoV-2 spike protein prevents rapid mutational escape seen with individual antibodies. Science 369, 1014–1018. https://doi.org/10.1126/science.abd0831.

30. Hansen, J., Baum, A., Pascal, K.E., Russo, V., Giordano, S., Wloga, E., Fulton, B.O., Yan, Y., Koon, K., Patel, K., et al. (2020). Studies in humanized mice and convalescent humans yield a SARS-CoV-2 antibody cocktail. Science 369, 1010–1014. https://doi.org/10.1126/science.abd0827.

31. Shi, R., Shan, C., Duan, X., Chen, Z., Liu, P., Song, J., Song, T., Bi, X., Han, C., Wu, L., et al. (2020). A human neutralizing antibody targets the receptor-binding site of SARS-CoV-2. Nature 584, 120–124. https://doi.org/10.1038/s41586-020-2381-y.

32. Cohen, M.S., Nirula, A., Mulligan, M.J., Novak, R.M., Marovich, M., Yen, C., Stemer, A., Mayer, S.M., Wohl, D., Brengle, B., et al. (2021). Effect of bamlanivimab vs placebo on incidence of COVID-19 among residents and staff of skilled nursing and assisted living facilities: a randomized clinical trial. JAMA 326, 46–55. https://doi.org/10.1001/jama.2021.8828.

33. Gottlieb, R.L., Nirula, A., Chen, P., Boscia, J., Heller, B., Morris, J., Huhn, G., Cardona, J., Mocherla, B., Stosor, V., et al. (2021). Effect of bamlanivimab as monotherapy or in combination with etesevimab on viral load in patients with mild to moderate COVID-19: a randomized clinical trial. JAMA 325, 632–644. https://doi.org/10.1001/jama.2021.0202.

34. Jones, B.E., Brown-Augsburger, P.L., Corbett, K.S., Westendorf, K., Davies, J., Cujec, T.P., Wiethoff, C.M., Blackbourne, J.L., Heinz, B.A., Foster, D., et al. (2021). The neutralizing antibody, LY-CoV555, protects against SARS-CoV-2 infection in nonhuman primates. Sci. Transl. Med. 13, eabf1906. https://doi.org/10.1126/scitranslmed.abf1906.

35. Dong, J., Zost, S.J., Greaney, A.J., Starr, T.N., Dingens, A.S., Chen, E.C., Chen, R.E., Case, J.B., Sutton, R.E., Gilchuk, P., et al. (2021). Genetic and structural basis for SARS-CoV-2 variant neutralization by a two-antibody cocktail. Nat. Microbiol. 6, 1233–1244. https://doi.org/10.1038/s41564-021-00972-2.

36. Zost, S.J., Gilchuk, P., Case, J.B., Binshtein, E., Chen, R.E., Nkolola, J.P., Schäfer, A., Reidy, J.X., Trivette, A., Nargi, R.S., et al. (2020). Potently neutralizing and protective human antibodies against SARS-CoV-2. Nature 584, 443–449. https://doi.org/10.1038/s41586-020-2548-6.

37. Barnes, C.O., West, A.P., Huey-Tubman, K.E., Hoffmann, M.A.G., Sharaf, N.G., Hoffman, P.R., Koranda, N., Gristick, H.B., Gaebler, C., Muecksch, F., et al. (2020). Structures of human antibodies bound to SARS-CoV-2 spike reveal common epitopes and recurrent features of antibodies. Cell 182, 828–842.e16. https://doi.org/10.1016/j.cell.2020.06.025.

38. Tortorici, M.A., Beltramello, M., Lempp, F.A., Pinto, D., Dang, H.V., Rosen, L.E., McCallum, M., Bowen, J., Minola, A., Jaconi, S., et al. (2020). Ultrapotent human antibodies protect against SARS-CoV-2 challenge via multiple mechanisms. Science 370, 950–957. https://doi.org/10.1126/science.abe3354.

39. Liu, L., Wang, P., Nair, M.S., Yu, J., Rapp, M., Wang, Q., Luo, Y., Chan, J.F.-W., Sahi, V., Figueroa, A., et al. (2020). Potent neutralizing antibodies against multiple epitopes on SARS-CoV-2 spike. Nature 584, 450–456. https://doi.org/10.1038/s41586-020-2571-7.

40. Barnes, C.O., Jette, C.A., Abernathy, M.E., Dam, K.-M.A., Esswein, S.R., Gristick, H.B., Malyutin, A.G., Sharaf, N.G., Huey-Tubman, K.E., Lee, Y.E., et al. (2020). SARS-CoV-2 neutralizing antibody structures inform therapeutic strategies. Nature 588, 682–687. https://doi.org/10.1038/s41586-020-2852-1.

41. Park, Y.-J., De Marco, A., Starr, T.N., Liu, Z., Pinto, D., Walls, A.C., Zatta, F., Zepeda, S.K., Bowen, J.E., Sprouse, K.R., et al. (2022). Antibody-mediated broad sarbecovirus neutralization through ACE2 molecular mimicry. Science 375, 449–454. https://doi.org/10.1126/science.abm8143.

42. Lei, C., Qian, K., Li, T., Zhang, S., Fu, W., Ding, M., and Hu, S. (2020). Neutralization of SARS-CoV-2 spike pseudotyped virus by recombinant ACE2-Ig. Nat. Commun. 11, 2070. https://doi.org/10.1038/s41467-020-16048-4.

43. Higuchi, Y., Suzuki, T., Arimori, T., Ikemura, N., Mihara, E., Kirita, Y., Ohgitani, E., Mazda, O., Motooka, D., Nakamura, S., et al. (2021). Engineered ACE2

receptor therapy overcomes mutational escape of SARS-CoV-2. Nat. Commun. *12*, 3802. https://doi.org/10.1038/s41467-021-24013-y.

44. Svilenov, H.L., Sacherl, J., Reiter, A., Wolff, L.S., Cheng, C.-C., Stern, M., Grass, V., Feuerherd, M., Wachs, F.-P., Simonavicius, N., et al. (2021). Picomolar inhibition of SARS-CoV-2 variants of concern by an engineered ACE2-IgG4-Fc fusion protein. Antiviral Res. *196*, 105197. https://doi.org/10.1016/j.antiviral.2021.105197.

45. Ferrari, M., Mekkaoui, L., Ilca, F.T., Akbar, Z., Bughda, R., Lamb, K., Ward, K., Parekh, F., Karattil, R., Allen, C., et al. (2021). Characterization of a novel ACE2-based therapeutic with enhanced rather than reduced activity against SARS-CoV-2 variants. J. Virol. *95*, e0068521. https://doi.org/10.1128/JVI.00685-21.

46. Chen, Y., Sun, L., Ullah, I., Beaudoin-Bussières, G., Anand, S.P., Hederman, A.P., Tolbert, W.D., Sherburn, R., Nguyen, D.N., Marchitto, L., et al. (2022). Engineered ACE2-Fc counters murine lethal SARS-CoV-2 infection through direct neutralization and Fc-effector activities. Sci. Adv. *8*, eabn4188. https://doi.org/10.1126/sciadv.abn4188.

47. Shekhar, M., Terashi, G., Gupta, C., Sarkar, D., Debussche, G., Sisco, N.J., Nguyen, J., Mondal, A., Vant, J., Fromme, P., et al. (2021). CryoFold: determining protein structures and data-guided ensembles from cryo-EM density maps. Matter *4*, 3195–3216. https://doi.org/10.1016/j.matt.2021.09.004.

48. Ikemura, N., Taminishi, S., Inaba, T., Arimori, T., Motooka, D., Katoh, K., Kirita, Y., Higuchi, Y., Li, S., Suzuki, T., et al. (2021). Engineered ACE2 counteracts vaccine-evading SARS-CoV-2 Omicron variant. Preprint at bioRxiv. https://doi.org/10.1101/2021.12.22.473804.

49. Zhang, L., Narayanan, K.K., Cooper, L., Chan, K.K., Devlin, C.A., Aguhob, A., Shirley, K., Rong, L., Rehman, J., Malik, A.B., et al. (2022). An engineered ACE2 decoy receptor can be administered by inhalation and potently targets the BA.1 and BA.2 omicron variants of SARS-CoV-2. Preprint at bioRxiv. https://doi.org/10.1101/2022.03.28.486075.

50. Wirnsberger, G., Monteil, V., Eaton, B., Postnikova, E., Murphy, M., Braunsfeld, B., Crozier, I., Kricek, F., Niederhöfer, J., Schwarzböck, A., et al. (2021). Clinical grade ACE2 as a universal agent to block SARS-CoV-2 variants. Preprint at bioRxiv. https://doi.org/10.1101/2021.09.10.459744.

51. Zhou, X.X., Bracken, C.J., Zhang, K., Zhou, J., Mou, Y., Wang, L., Cheng, Y., Leung, K.K., and Wells, J.A. (2020). Targeting phosphotyrosine in native proteins with conditional, bispecific antibody traps. J. Am. Chem. Soc. *142*, 17703–17713. https://doi.org/10.1021/jacs.0c08458.

52. Koerber, J.T., Thomsen, N.D., Hannigan, B.T., Degrado, W.F., and Wells, J.A. (2013). Nature-inspired design of motif-specific antibody scaffolds. Nat. Biotechnol. *31*, 916–921. https://doi.org/10.1038/nbt.2672.

53. Mou, Y., Zhou, X.X., Leung, K., Martinko, A.J., Yu, J.-Y., Chen, W., and Wells, J.A. (2018). Engineering improved antiphosphotyrosine antibodies based on an immunoconvergent binding motif. J. Am. Chem. Soc. *140*, 16615–16624. https://doi.org/10.1021/jacs.8b08402.

54. Weidenbacher, P.A.-B., Waltari, E., de los Rios Kobara, I., Bell, B.N., Pak, J.E., and Kim, P.S. (2022). Converting non-neutralizing SARS-CoV-2 antibodies targeting conserved epitopes into broad-spectrum inhibitors through receptor blockade. Preprint at bioRxiv. https://doi.org/10.1101/2022.01.24.477625.

55. Punjani, A., Rubinstein, J.L., Fleet, D.J., and Brubaker, M.A. (2017). cryoSPARC: algorithms for rapid unsupervised cryo-EM structure determination. Nat. Methods *14*, 290–296. https://doi.org/10.1038/nmeth.4169.

56. Zheng, S.Q., Palovcak, E., Armache, J.-P., Verba, K.A., Cheng, Y., and Agard, D.A. (2017). MotionCor2: anisotropic correction of beam-induced motion for improved cryo-electron microscopy. Nat. Methods *14*, 331–332. https://doi.org/10.1038/nmeth.4193.

57. Mastronarde, D.N. (2005). Automated electron microscope tomography using robust prediction of specimen movements. J. Struct. Biol. *152*, 36–51. https://doi.org/10.1016/j.jsb.2005.07.007.

58. Mastronarde, D.N. (2003). Serialem: a program for automated tilt series acquisition on tecnai microscopes using prediction of specimen position. Microsc. Microanal. *9*, 1182–1183. https://doi.org/10.1017/S1431927603445911.

59. Grant, T., Rohou, A., and Grigorieff, N. (2018). cisTEM, user-friendly software for single-particle image processing. Elife *7*, e35383. https://doi.org/10.7554/eLife.35383.

60. Pettersen, E.F., Goddard, T.D., Huang, C.C., Couch, G.S., Greenblatt, D.M., Meng, E.C., and Ferrin, T.E. (2004). UCSF Chimera—a visualization system for exploratory research and analysis. J. Comput. Chem. *25*, 1605–1612. https://doi.org/10.1002/jcc.20084.

61. Liebschner, D., Afonine, P.V., Baker, M.L., Bunkóczi, G., Chen, V.B., Croll, T.I., Hintze, B., Hung, L.W., Jain, S., McCoy, A.J., et al. (2019). Macromolecular structure determination using X-rays, neutrons and electrons: recent developments in Phenix. Acta Crystallogr. D Struct. Biol. *75*, 861–877. https://doi.org/10.1107/S2059798319011471.

62. Alford, R.F., Leaver-Fay, A., Jeliazkov, J.R., O'Meara, M.J., DiMaio, F.P., Park, H., Shapovalov, M.V., Renfrew, P.D., Mulligan, V.K., Kappel, K., et al. (2017). The Rosetta all-atom energy function for macromolecular modeling and design. J. Chem. Theory Comput. *13*, 3031–3048. https://doi.org/10.1021/acs.jctc.7b00125.

63. Leman, J.K., Weitzner, B.D., Lewis, S.M., Adolf-Bryfogle, J., Alam, N., Alford, R.F., Aprahamian, M., Baker, D., Barlow, K.A., Barth, P., et al. (2020). Macromolecular modeling and design in Rosetta: recent methods and frameworks. Nat. Methods *17*, 665–680. https://doi.org/10.1038/s41592-020-0848-2.

64. Emsley, P., Lohkamp, B., Scott, W.G., and Cowtan, K. (2010). Features and development of coot. Acta Crystallogr. D Biol. Crystallogr. *66*, 486–501. https://doi.org/10.1107/S0907444910007493.

65. Croll, T.I. (2018). ISOLDE: a physically realistic environment for model building into low-resolution electron-density maps. Acta Crystallogr. D Struct. Biol. *74*, 519–530. https://doi.org/10.1107/S2059798318002425.

66. Kucukelbir, A., Sigworth, F.J., and Tagare, H.D. (2014). Quantifying the local resolution of cryo-EM density maps. Nat. Methods *11*, 63–65. https://doi.org/10.1038/nmeth.2727.

67. Tan, Y.Z., Baldwin, P.R., Davis, J.H., Williamson, J.R., Potter, C.S., Carragher, B., and Lyumkis, D. (2017). Addressing preferred specimen orientation in single-particle cryo-EM through tilting. Nat. Methods *14*, 793–796. https://doi.org/10.1038/nmeth.4347.

68. Pintilie, G., Zhang, K., Su, Z., Li, S., Schmid, M.F., and Chiu, W. (2020). Measurement of atom resolvability in cryo-EM maps with Q-scores. Nat. Methods *17*, 328–334. https://doi.org/10.1038/s41592-020-0731-1.

69. Weinberg, Z.Y., Hilburger, C.E., Kim, M., Cao, L., Khalid, M., Elmes, S., Diwanji, D., Hernandez, E., Lopez, J., Schaefer, K., et al. (2021). Sentinel cells enable genetic detection of SARS-CoV-2 Spike protein. Preprint at bioRxiv. https://doi.org/10.1101/2021.04.20.440678.

70. Punjani, A., Zhang, H., and Fleet, D.J. (2020). Non-uniform refinement: adaptive regularization improves single-particle cryo-EM reconstruction. Nat. Methods *17*, 1214–1221. https://doi.org/10.1038/s41592-020-00990-8.

71. Laurie, M.T., Liu, J., Sunshine, S., Peng, J., Black, D., Mitchell, A.M., Mann, S.A., Pilarowski, G., Zorn, K.C., Rubio, L., et al. (2021). SARS-CoV-2 variant exposures elicit antibody responses with differential cross-neutralization of established and emerging strains including Delta and Omicron. Preprint at medRxiv. https://doi.org/10.1101/2021.09.08.21263095.

72. Hoffmann, M., Kleine-Weber, H., and Pöhlmann, S. (2020). A multibasic cleavage site in the spike protein of SARS-CoV-2 is essential for infection of human lung cells. Mol. Cell *78*, 779–784.e5. https://doi.org/10.1016/j.molcel.2020.04.022.

73. Laurie, M.T., Liu, J., Sunshine, S., Peng, J., Black, D., Mitchell, A.M., Mann, S.A., Pilarowski, G., Zorn, K.C., Rubio, L., et al. (2022). SARS-CoV-2 variant exposures elicit antibody responses with differential cross-neutralization of established and emerging strains including delta and omicron. J. Infect. Dis. *225*, 1909–1914. https://doi.org/10.1093/infdis/jiab635.

STAR★METHODS

KEY RESOURCES TABLE

REAGENT or RESOURCE	SOURCE	IDENTIFIER
Bacterial and virus strains		
WT-Spike (D614G) (based on SARS-CoV-2 B.1 strain) WT-Spike pseudovirus	This study	N/A
Delta-Spike (based on SARS-CoV-2 B.1.617.2 strain) Delta-Spike pseudovirus	This study	N/A
Omicron-Spike (based on SARS-CoV-2 BA.1 strain) Omicron-Spike pseudovirus	This study	N/A
XL10-Gold® Ultracompetent cells	Agilent	N/A
Chemicals, peptides, and recombinant proteins		
Spike protein	This study	S protein
ACE2 computationally engineered protein	This study	CVD293
ACE2 affinity matured protein	This study	CVD313
ACE2 linker variant of CVD313	This study	CVD432
WT-RBD	This study	WT-RBD
Delta-Spike-RBD	This study	Delta-Spike-RBD
Omicron-Spike-RBD	This study	Omicron-Spike-RBD
Deposited data		
Spike-RBD/CVD293 cryo-EM map	This study	EMD: 27731
Spike-RBD/CVD293 model	This study	PDB: 8DV2
Spike-RBD/CVD432 cryo-EM map	This study	EMD: 27730
Spike-RBD/CVD432 model	This study	PDB: 8DV1
S protein/CVD293 (1-RBD-up state) cryo-EM map	This study	EMD: 27731
S protein/CVD432 (1-RBD-up state) cryo-EM map	This study	EMD: 27730
S protein/CVD432 (2-RBD-up state) cryo-EM map	This study	EMD: 27730
Experimental models (Cell lines)		
ExpiCHO-S™	ThermoFisher Scientific	N/A
Expi293F™	ThermoFisher Scientific	N/A
Huh7.5.1-ACE2-TMPRSS2	Gift from Andreas Puschnik	N/A
Recombinant DNA		
S protein	Gift from Pak lab and Krammer lab	S protein
ACE2 computationally engineered protein	Glasgow et al.[13]	CVD293
ACE2 affinity matured protein	Glasgow et al.[13]	CVD313
ACE2 linker variant of CVD313	Twist Biosciences	CVD432
WT-RBD	Glasgow et al.[13]	WT-RBD
Delta-Spike-RBD	This study	Delta-Spike-RBD
Omicron-Spike-RBD	This study	Omicron-Spike-RBD
Oligonucleotides		
Delta-Spike-RBD Forward - TGGCGCTGGTGACCAACAGCACT AGTCGCTTCCCCAATATCACCAAC Reverse -GCTCCAGCTACCGTGTGCGGTCC GAAAAAGTCAACCAATCT	This study	Delta-Spike-RBD

(Continued on next page)

Continued

REAGENT or RESOURCE	SOURCE	IDENTIFIER
Omicron-Spike-RBD Forward - TGGCGCTGGTGACCAACAGCACT AGTCGCTTCCCCAATATCACCAAC Reverse - CCAAAGAAGAGCACCAATCTGAC TAGTTCTGGTGGTGGTGGT	This study	Omicron-Spike-RBD
Software and algorithms		
cryoSPARC	Punjani et al.[55]	https://cryosparc.com
MotionCor2	Zheng et al.[56]	https://docs.google.com/forms/d/e/1FAIpQLSfAQm5MA81qTx90W9 JL6ClzSrM77tytsvyyHh1ZZWrFByh mfQ/viewform
SerialEM	Mastronarde,[57,58]	https://bio3d.colorado.edu/SerialEM/
cisTEM	Grant et al.[59]	https://cistem.org/
CHIMERA	Pettersen et al.[60]	https://www.cgl.ucsf.edu/chimera/
Phenix Real Space Refine	Liebschner et al.[61]	https://phenix-online.org
Rosetta (2020.08 release) For automated structure refinement	Wang et al.[19]	https://www.rosettacommons.org/software
Rosetta version 2021.48.post.dev+8.master. 77491fa20be 77491fa20be83588cfc37ab422 ba5b95eca128eb git@github.com:Rosetta Commons/main.git 2021-12-02T08:56:13 Protein design and structural analysis	Alford et al. and Leman et al.[62,63]	https://www.rosettacommons.org/software
COOT 0.9	Emsley et al.[64]	https://www2.mrc-lmb.cam.ac.uk/personal/pemsley/coot/
ISOLDE 1.0	Croll,[65]	https://isolde.cimr.cam.ac.uk/static/isolde/doc/tutorials/intro/cryo_intro/cryo_intro.html
ResMap	Kucukelbir et al.[66]	http://resmap.sourceforge.net
3DFSC server	Tan et I.[67]	https://3dfsc.salk.edu
Q-scores	Pintilie et al.[68]	https://github.com/gregdp/mapq
FlowJo™	BD Biosciences	https://www.flowjo.com
Octet Data Analysis HT software version 10.0	Sartorius	https://www.sartorius.com/en/products/protein-analysis/octet-systems-software
GraphPad Prism 9 Version 9.3.0 (345)	Graphpad (Dotmatics)	https://www.graphpad.com/scientific-software/prism/

RESOURCE AVAILABILITY

Lead contact

Further information and requests for resources and reagents should be directed to and will be fulfilled by the lead contact, Kliment A. Verba (kliment.verba@ucsf.edu).

Materials availability

All reagents generated in this study are available from the lead contact with a completed materials transfer agreement.

Data and code availability

All standardized cryo-EM datasets generated in this study have been deposited in the PDB and EMDB and are publicly available as of the date of publication. The PDB and EMDB accession numbers are provided in the key resources table. All original code generated in this study is provided in the Supplementary Appendix. Any additional information required to reanalyze the data reported in the paper is available from lead contact upon request.

EXPERIMENTAL MODEL AND SUBJECT DETAILS

Bacterial strains

XL10-Gold® Ultracompetent cells were purchased from Agilent (Catalog number: 200314) and were used to obtained purified DNA.

Cell lines

ExpiCHO-S™ (ThermoFisher Scientific, Catalog number: A29127) and Expi293F™ (ThermoFisher Scientific, Catalog number: A14527) cells were used to produce recombinant proteins. Both cell lines were maintained according to the manufacturer recommended protocol until transfection. ExpiCHO-S™ (1ml, 1x10^{7}cells) were directly thawed into 25ml of prewarmed ExpiCHO™ expression media and allowed to revive for 2-3 days. The cells were passaged every 3-4 days to maintain density at or below 4x10^6 - 6x10^6 viable cells/ml. ExpiCHO-S™ cells were maintained at 37°C, 8% CO2 and 125 +/- 5rpm. Expi293F™ (1ml, 1x10^{7}cells) were directly thawed into 25ml of prewarmed Expi293™ expression media and allowed to revive for 2-3 days. The cells were passaged every 3-4 days to maintain density at or below 3x10^6 - 5x10^6 viable cells/ml. Expi293F™ cells were maintained at 37°C, 8% CO2 and 125 +/- 5rpm

Huh7.5.1-ACE2-TMPRSS2 cell line was a gift from Andreas Puschnik. 1x10^7- 1.5x10^7 cells were thawed directly into prewarmed complete culture media (Dulbecco's Modified Eagle's Medium with 10% fetal bovine serum, 10mM HEPES, 1 × Pen-Strep-Glutamine). The cells were allowed to revive for 2-3 days and were passaged once they reached >70-80% confluence and were maintained at >95% viability in complete culture media. Huh7.5.1-ACE2-TMPRSS2 cells were maintained at 37°C and 5% CO2.

METHOD DETAILS

Cloning, expression and purification of protein constructs

S protein plasmid was a generous gift from the Pak lab (Chan Zuckerberg Initiative Biohub) and Krammer lab (Icahn School of Medicine at Mount Sinai). S protein construct has an N-terminal spike protein signal peptide, a trimerization domain and C-terminal 6XHis-tag. WT, Delta-, Omicron-SARS-CoV-2 spike RBD and ACE2 variants (CVD293) were cloned into a pFUSE-based vector with Zeocin antibiotic resistance marker for mammalian expression using the Gibson method. The SARS-CoV-2 spike RBD construct has an IL2 secretion signal followed by the gene of interest, a Gly-Ser linker, a TEV protease cut site, a Gly-Ser linker, an 8X His-tag and an Avi-tag. CVD293 was cloned into a similar construct with N-terminal IL2 secretion signal followed by ACE2 with the relevant mutations (K31F, H34I, E35Q), a Gly-Ser linker, a TEV protease cut site, a Gly-Ser linker, a human IgG1 hinge and Fc, and AviTag. Construct CVD432 was purchased from Twist Bioscience (www.twistbioscience.com). The construct has an Ampicillin resistance marker, an N-terminal ACE2 secretion signal followed by ACE2 with the relevant CVD313 mutations (K31F, N33D, H34S, E35Q), a short Gly-Ser linker, a human IgG1 hinge and Fc. Also, the H345L mutation in CVD313 was reverted to wildtype residue, histidine.

S protein (residues 1-1208, RRAR to GSAS mutation at residues 682-685 and KV to PP mutations at residues 986-987) was purified based on the previously described protocol.[69] 30ml of ExpiCHO-S™ (ThermoFisher Scientific, Catalog number: A29127) cells at 6M cells/mL were transfected with 1ug/mL of the spike WT using the ExpiCHO™ Expression System Kit (Gibco, catalog # A29133) following the manufacturer's Standard protocol. Briefly, the transfected cells were shaken at 37°C and 8% CO$_2$ and 18 hours post-transfection, the cultures were supplemented with ExpiCHO™ Feed and ExpiFectamine™ CHO Enhancer and continued to be shaken at 37°C and 8% CO$_2$ for up to 10 days. The supernatant with secreted spike protein was collected by centrifugation of the culture at 4000xG for 15 mins. The media was filtered using a 0.42µM filter and was transferred to a 50 mL centrifuge tube. The sample was then mixed with 2 mL washed Ni-Excel resin (Millipore Sigma, catalog # GE17371201) pre-equilibrated with 10 mM Tris/HCl, pH 8.0, 200 mM NaCl and placed on a rocker for 1 hour at room temperature. After binding, the sample was washed with 25 bed volumes of Wash buffer (10 mM Tris/HCl, pH 8.0, 200 mM NaCl, 10 mM imidazole), and eluted with 7 bed volumes of elution buffer (10 mM Tris pH 8.0, 200 mM NaCl, 500 mM imidazole) into separate 2 mL centrifuge tubes. The eluent was concentrated, filtered, and a final SEC polishing step was performed on Superose® 6 10/300 Increase (Millipore Sigma, catalog # GE17-5172-01) pre-equilibrated in 10 mM HEPES pH 8.0, 200 mM NaCl at 4°C.

WT, Delta-, Omicron-SARS-CoV-2 spike RBD and ACE2 variants (CVD293 and CVD432) were expressed in high density Expi293F™ (ThermoFisher Scientific, Catalog number: A14527) cells in Expi293™ expression media following manufacturer's protocol (Expi293 Expression System, ThermoFisher Scientific, Catalog number: A14635). Briefly, 3x10^6 cell/ml at >95% viability in 25ml media were transfected with ~30ug of DNA using ExpiFectamine™ transfection reagent and Opti-MEM™ I medium. The transfected cells were incubated at 37°C, 8% CO$_2$ on an orbital shaker, supplemented with ExpiFectamine™ 293 Transfection Enhancer 1 and ExpiFectamine™ 293 Transfection Enhancer 2 about 18-22 hours post-transfection and continued to be incubated at 37°C, 8% CO$_2$ on an orbital shaker for additional 4-5 days. Cells were harvested 4-5 days post-transfection, centrifuged at 3000 x g for 15 minutes, supernatant collected and filtered through 0.22µM syringe filter. Proteins were neutralized with 10X phosphate buffered saline (PBS, 0.01 M phosphate buffer, 0.0027 M KCl and 0.137 M NaCl, Millipore Sigma P4417-100TAB), pH 7.4 to a final concentration of 2.5x PBS (342.5 mM NaCl, 6.75 mM KCl and 29.75 mM phosphates). SARS-CoV-2 RBDs were purified using cobalt-based immobilized metal affinity chromatography followed by buffer exchange into 1X PBS using a Superdex 200 Increase 10/300 GL column (Cytiva). Fc-fused ACE2 proteins were purified on HiTrap Protein A column (GE Healthcare) and eluted with 50 mM Tris pH 7.2, 4 M MgCl$_2$ and buffer exchanged into 1X PBS. The protein concentrations were estimated based on the protein absorbance at 280 nm with a spectrophotometer (Nanodrop One, Thermo).

All the proteins were >95% pure as determined by SDS-Page gel electrophoresis. The proteins were aliquoted, flash frozen, and stored in -80°C.

Cryo-electron microscopy sample preparation and data collection

Purified S protein at 2 μM was mixed with either CVD293 (at 2.5 μM) or CVD432 (at 3 μM) just prior to plunge freezing. 300 mesh 1.2/1.3R UltrAufoil grids were glow discharged at 15 mA for 30 seconds. Vitrification was done using FEI Vitrobot Mark IV (ThermoFisher) set up at 4°C and 100% humidity. 4 μl complex sample was applied to the grids and the blotting was performed with a blot force of 0 for 4 s prior to plunge freezing into liquid ethane. For S protein/CVD293 complex, two datasets comprising of 2,058 and 3,636 120-frame super-resolution movies each were collected while for S protein/CVD432 complex, three datasets comprising of 4,915, 3,196, and 2,574 120-frame super-resolution movies each were collected. For both complexes movies were acquired in super-resolution mode on a Titan Krios (ThermoFisher) equipped with a K3 camera and a Bioquantum energy filter (Gatan) set to a slit width of 20 eV. Collection was performed with a 3x3 image shift at a calibrated magnification of 105, 000 x corresponding to a pixel size of 0.4265 Å/pix. Collection dose rate was 8 e⁻/pixel/second for a total dose of 68 e⁻/Å2. Defocus range was -0.8 to -1.8 μm. Movies were subsequently corrected for drift using MotionCor2[56] and were Fourier-cropped by a factor of 2 to a final pixel size of 0.834 Å/pixel. Each collection was performed with semi-automated scripts in SerialEM.[57,58]

Data processing

S protein/CVD293 complex 1-RBD-up state (Figure S2). Initial processing was done in cryoSPARC (v2.15.0).[55,70] The two datasets with 3636 and 2058 dose-weighted motion corrected micrographs[56] were imported and Patch CTF(M) was performed. Micrographs were curated based on CTF-fit resolution (<4 Å), ice-thickness, and presence of carbon. After manual curation, 3144 and 1575 micrographs were selected for further processing. Blob-picker was used to pick 1,673,305 and 831,773 particles and extraction was done with a box size of 580 px downsized to 480 px for each dataset. 2D-classification was done into 150 classes and good classes were selected with a total of 401,671 particles combined from both datasets. Multiple rounds of heterogeneous, homogenous, and non-uniform refinements in cryoSPARC and focused classification in cisTEM[59] resulted in a 3.77 Å 3D-reconstruction of S protein/CVD293 with 61,033 particles. Particle subtraction/local refinement was performed on this final stack of particles to obtain a 3.77 Å 3D reconstruction of WT-RBD (residues 331-541)/CVD293 (residues 18-614).

S protein/CVD432 complex 1-RBD-up state (Figure S3). Initial processing was done in cryoSPARC (v2.15.0). The three datasets with 4915, 3916 and 2574 dose-weighted motion corrected micrographs were imported and Patch CTF(M) was performed. Micrographs were curated based on CTF-fit resolution (<4 Å), ice-thickness, and presence of carbon. After manual curation, 3864, 2238 and 2148 micrographs were selected for further processing. Blob-picker was used to pick 1,259,441 particles from Dataset 1 while template-based particle picker (260 Å diameter) was used to pick 782,620 and 752,648 particles for Dataset 2 and Dataset 3, respectively. Extraction was done with a box size of 512 px for Dataset 1 which was re-extracted with box size of 600 px after a round of ab-initio refinement and finally downsampled to 400 px. For Datasets 2 and 3, extraction was done at box size 600 px and then downsampled to 400 px. 2D-classification was done with 150 classes for each dataset and good classes of S protein/CVD432 in 1-RBD-up state were selected with a total of 601,624 particles combined from the three datasets. Multiple rounds of heterogeneous, non-uniform refinements and homogenous refinements in cryoSPARC and focused classification in cisTEM resulted in a 3.5 Å 3D-reconstruction of S protein/CVD432 1-RBD-up state with 97,082 particles. Particle subtraction/local refinement was performed on this final stack of particles to obtain a 3.4 Å 3D reconstruction of WT-RBD (residues 331-541)/CVD432 (residues 18-614).

S protein/CVD432 complex 2-RBD-up state (Figure S4). We processed the S protein/CVD432 complex 2-RBD-up state independent of the 1-RBD-up state. Initial processing was done in cryoSPARC (v2.15.0). The three datasets with 4915, 3916 and 2574 dose-weighted motion corrected micrographs were imported and Patch CTF(M) was performed. Micrographs were curated based on CTF-fit resolution (<4 Å), ice-thickness, and presence of carbon. After manual curation, 3833, 2253 and 2175 micrographs were selected for further processing. We first used blob-picker on Dataset 1 to pick 1,597,143 and after 2D classification, 19 good classes were selected. The 19 classes from Data set 1 were used for template-based particle picker (220 Å diameter) to pick 1,499,401 and 1,019,564 and 1,328,287 particles for Dataset 1, Dataset 2 and Dataset 3, respectively. Extraction was done at box size 600 px for all datasets. 2D-classification was done into 150 classes for each dataset and good looking classes with S protein/CVD432 in 2-RBD-up state were selected with a total of 113,836 particles combined from the three datasets. Multiple rounds of heterogeneous, non-uniform refinements and homogenous refinements in cryoSPARC and focused classification in cisTEM resulted in a 2.97 Å 3D-reconstruction of S protein/CVD432 2-up state with 97,374 particles. Each WT-RBD/CVD432 interface in the 2-RBD-up state was at an overall low resolution and particle subtraction/local refinement was not performed.

Model building and refinement

Low resolution rigid body fitting. 1-RBD-up state S protein/WT-ACE2 model with PDB ID: 7DX5, was used as the initial model for rigid body fitting into cryo-EM density map of 1-RBD-up state of S protein/CVD293 or 1-RBD-up state of S protein/CVD432 in CHIMERA.[60] For 2-RBD-up state of S protein/CVD432, we generated a model by rigid body fitting PDB ID: 7DX5 into the density map and simultaneously rigid body fitting WT-RBD/ACE2 (18-614) complex with PDB ID: 6M0J into the second RBD-up region of the map in CHIMERA. The final model was torion relaxed with Rosetta into the S protein/WT-ACE2 2-RBD-up state cryo-EM map. Rosetta into the Overall, the fits agree with previously reported 1-RBD-up states for S protein/ACE2 (18-614) complexes.

High resolution "final consensus" model building
High resolution map of WT-RBD/CVD293 (18-614) with mutations K31F, H34I, E35Q or WT-RBD/CVD432 (18-614) with mutations K31F, N33D, H34S, E35Q were generated from S protein/CVD293 map or S protein/CVD432 map, respectively, in cryoSPARC (v2.15.0) by Particle subtraction/Local refinement. PDB ID: 6M0J was used for initial rigid body fit into the WT-RBD/CVD293 (18-614) map. This model was then refined against the respective maps in Phenix Real Space Refine[61] with the corrected sequence input for CVD293 or CVD432. This was followed by a FastRelax in torsion space with Rosetta (2020.08 release).[19] Model for each complex was manually examined and corrected using COOT 0.9[64] and ISOLDE 1.0.[65] At this point glycans were added to the model manually in Chimera and COOT and then were refined using another round of Rosetta FastRelax followed by examination/final polish in ISOLDE. The B-factors were assigned using a Rosetta B-factor fitting mover. Local resolution was determined by running the ResMap program.[66] Directional FSC curves were determined by submitting the associated files to the 3DFSC server.[67] Q-scores were calculated using the Q-score plugin for USCF Chimera.[68]

Multi-model pipeline
The Cryo-EM consensus model of WT-RBD/CVD293 (18-614) or WT-RBD/CVD432 (18-614) was used as the starting model for the pipeline. We applied the Rosetta Iterative Rebuild protocol on 10-amino acid overlapping stretches of the interface helix for each consensus model. The parameters used were defined in an XML file (Parameters.xml) found in SI Appendix: Methods S1. For each 10-amino acid stretch of the interface helix we generated 2000 independent models totaling 8000 models for the entire interface helix from ACE2 residue 21 to residue 52. Total of 200 models were then selected based on the total Rosetta energy score followed by the top 20 that best fit to the map destiny. A total of 80 top selected models for each complex were then used for further analyses. We calculated the local average per residue average side-chain RMSD in CHIMERA and average interface energy (in REU) for the residues of the interface helix.

Energy calculations
Total and individual pairwise interface energies were calculated for all design models and cryo-EM atomic models using the Rosetta interface energy application. Per-residue energies were calculated using the Rosetta per-residue energy application, and total energies were calculated using the Rosetta scoring application in Rosetta (2021.48.post.dev+8.master.77491fa20be77491fa20be83588cfc 37ab422ba5b95eca128ebgit@github.com:RosettaCommons/main.git 2021-12-02T08:56:13)[62,63]. For the cryo-EM atomic models of CVD293 and CVD432, all scores were averaged and standard deviations were calculated. The command lines and code are available in the SI Appendix: Methods S1. The average interface energies and standard deviations (shown as error bars) calculated across all 80 cryo-EM-based models are shown in Figure 3E and broken down by residue in Figure S6. All the code involved in these calculations, and all the analysis code, is available at https://github.com/anumazam/ACE2_traps.

Design models of the ACE2 domain of CVD432
Design models of the ACE2 domain of CVD432 were generated using the RosettaScripts framework.[13] Beginning with the atomic models of CVD293 solved by cryo-EM using the multi-model pipeline, we mutated N33 and I34 to aspartic acid and serine, respectively, in each of the 80 WT-RBD/CVD293 cryo-EM based models and minimized the complexes. Total energies and interface energies were calculated as described in "energy calculations." The average interface energies and standard deviations (shown as error bars) calculated across all 80 design models are shown in Figure 3E. The code is available in the SI Appendix: Methods S1.

Determination of binding affinity using biolayer interferometry (BLI)
Affinity measurements were carried out at room temperature using an Octet RED384 system. In our BLI experiments, ACE2 Fc-fusions are tethered to either Streptavidin biosensors (WT-ACE2, CVD293) (Sartorius®, Item no.: 18-5019) or ProtA biosensors (Sartorius®, Item no.: 18-5010) and WT, Delta-, Omicron-SARS-CoV-2 spike RBD are present as the analyte in solution in a 384-well microplate. The biosensors were washed in phosphate buffered saline (1X PBS) with 0.05% Tween-20 at pH 7.4 and 0.2% bovine serum albumin (BSA) (1X PBSTB) for 200 seconds. Antigens WT-ACE2, CVD293 were diluted to 10 nM in 1X PBSTB containing 10 μM biotin (1X PBSTBB) as blocking agent while antigen CVD432 was diluted 10nM in 1X PBSTB. The antigens were then loaded to the respective biosensors for 300 seconds. Following loading, a baseline was established by washing the WT-ACE2 or CVD293 bound Streptavidin biosensors in 1X PBSTBB and CVD432 bound ProtA biosensors in 1X PBSTB for 200 seconds. WT, Delta-, Omicron-SARS-CoV-2 spike RBD were then allowed to associate with the antigen at concentrations ranging from 0 to 25 nM of Spike for about 600 seconds and then returned to the respective washing well to follow dissociation for about 900 seconds. Raw data were fit in Octet Data Analysis HT software version 10.0 using curve-fitting kinetic analysis with global fitting and assuming 1:1 non-cooperative binding kinetics. All fits to BLI data had R^2 (goodness of fit) > 0.90.

Pseudovirus production
SARS-CoV-2 pseudoviruses bearing spike proteins of variants of interest were generated as previously described[71–73] using a recombinant vesicular stomatitis virus (VSV) expressing green fluorescent protein (GFP) in place of the VSV glycoprotein (rVSV Δ G-GFP). B.1 (WT, 1 spike mutation (D614G)), B.1.617.2/delta (9-10 spike mutations), and BA.1/ omicron (37 spike mutations) were cloned in a cytomegalovirus enhancer-driven expression vector and used to produce SARS-CoV-2 spike pseudoviruses.

The mutations for each variant are listed in Table S4. Pseudoviruses were titered on Huh7.5.1 cells overexpressing ACE2 and TMPRSS2 (gift of Andreas Puschnik) using GFP expression to measure the concentration of focus forming units (ffu).

Pseudovirus neutralization assay

Pseudovirus Neutralization Assay was performed as described previously[71,73] Huh7.5.1-ACE2-TMPRSS2 cells were seeded in 96-well plates at a density of 7000-8000 cells/well 1 day prior to pseudovirus infection. ACE2 receptor traps were serially diluted into complete culture media (Dulbecco's Modified Eagle's Medium with 10% fetal bovine serum, 10mM HEPES, 1X Pen-Strep-Glutamine). Each pseudovirus was diluted to 125 ffu/μL and 30 μL of each pseudovirus was mixed with $\sim$30 μL of ACE2 receptor traps or media only. Media only with no pseudovirus served as an additional control. These were incubated at 37°C for 1 hour before adding 50 μL of virus:binder incubated mix directly to previously plated cells. Cells inoculated with ACE2 receptor traps/pseudovirus mixtures were incubated at 37°C and 5% CO2 for 24 hours. The cells were then lifted and resuspended using 20 μL of 10X TrypLE Select (Gibco) and GFP signal of infected cells recorded using Beckman CytoFlex Cytometer B4R3V4.

Data were analyzed with FlowJo™ to determine percent GFP-positive pseudovirus transduced cells. GFP-signals from wells with no ACE2 receptor traps (media only with pseudovirus) were used to normalize the data and determine percent neutralization. A 7-8 point dose-response curve was generated in GraphPad Prism and IC50s reported in μg/mL. The reported IC50s are based on two technical and biological replicates for each pseudovirus/ACE2 receptor trap pair.

QUANTIFICATION AND STATISTICAL DETAILS

Statistical details of individual experiments can be found in corresponding figure legends and method details. Mean and standard deviation for Figures 4D and S1D were calculated in GraphPad Prism 9 Version 9.3.0 (345), and in Microsoft Excel for Figures 3E and S6.